FABRICATION AND CHARACTERIZATION OF HIGH-SPEED, HIGH QUANTUM EFFICIENCY, RESONANT CAVITY ENHANCED SCHOTTKY PHOTODIODES

A THESIS
SUBMITTED TO THE DEPARTMENT OF PHYSICS
AND THE INSTITUTE OF ENGINEERING AND SCIENCE
OF BILKENT UNIVERSITY
IN PARTIAL FULFILLMENT OF THE REQUIREMENTS
FOR THE DEGREE OF
DOCTOR OF PHILOSOPHY

By
Erhan Polatkan Ata
10 July 1998

FABRICATION AND CHARACTERIZATION OF HIGH-SPEED, HIGH QUANTUM EFFICIENCY, RESONANT CAVITY ENHANCED SCHOTTKY PHOTODIODES

A THESIS

SUBMITTED TO THE DEPARTMENT OF PHYSICS

AND THE INSTITUTE OF ENGINEERING AND SCIENCE

OF BİLKENT UNIVERSITY

IN PARTIAL FULFILLMENT OF THE REQUIREMENTS

FOR THE DEGREE OF

DOCTOR OF PHILOSOPHY

By

Erhan Polatkan Ata

10 July 1998

I certify that I have read this thesis and that in my opinion it is fully adequate, in scope and in quality, as a dissertation for the degree of Doctor of Philosophy.

Assoc. Prof. Ekmel Özbay (Supervisor)

I certify that I have read this thesis and that in my opinion it is fully adequate, in scope and in quality, as a dissertation for the degree of Doctor of Philosophy.

Assoc. Prof. Çiğdem Erçelebi

I certify that I have read this thesis and that in my opinion it is fully adequate, in scope and in quality, as a dissertation for the degree of Doctor of Philosophy.

Prof. Cemal Yalabık

I certify that I have read this thesis and that in my opinion it is fully adequate, in scope and in quality, as a dissertation for the degree of Doctor of Philosophy.

Assoc. Prof. Orhan Aytür

I certify that I have read this thesis and that in my opinion it is fully adequate, in scope and in quality, as a dissertation for the degree of Doctor of Philosophy.

Assist. Prof. Ali Serpengüzel

Approved for the Institute of Engineering and Science:

Prof. Mehmet Baray,
Director of Institute of Engineering and Science

Abstract

FABRICATION AND CHARACTERIZATION OF HIGH-SPEED, HIGH QUANTUM EFFICIENCY, RESONANT CAVITY ENHANCED SCHOTTKY PHOTODIODES

Erhan Polatkan Ata
Ph. D. in Physics
Supervisor: Assoc. Prof. Ekmel Özbay
10 July 1998

Rapidly developing "photonics" technology promises higher bandwidths of communication than any other technique did ever. The increasing rate of communication not only alters science and technology, but brings a global cultural exchange, which seems to be one of the most important revolutions in the history.

Photodetectors, as vital components of optoelectronics, are still being developed to achieve satisfying performances for the increasing communication demands. We have designed and fabricated high-speed, high efficiency resonant cavity enhanced (RCE) Schottky photodiodes, suitable for 800-850 nm operation wavelengths. We have used two different GaAs/AlGaAs based epitaxial structures to achieve high performance. From one of these structures, we fabricated photodiodes with 50% quantum efficiency and 80 GHz 3-dB bandwidth. The other structure had a design suitable for prefabrication wavelength tuning and adjustable active layer thickness. On this structure, we achieved 20% quantum efficiency along with, world record for RCE photodiodes, over 110 GHz 3-dB estimated bandwidth.

We investigated effects of active layer, top Au layer, and silicon nitride coating layer thicknesses on the RCE devices. Discrepancy between theory and experiments were also explained briefly.

Methods for improving performances of photodiodes has been proposed as possible future work. Possible applications, which may make use of current know-how on the subject, have also been mentioned.

Keywords: Resonant Cavity, Resonant Cavity Enhancement, Photodiode, Schottky Contact, Schottky Photodiode, Quantum Efficiency, High-Speed.

Özet

RESONANT KAVİTE İLE GÜÇLENDİRİLMİŞ, YÜKSEK HIZLI VE YÜKSEK VERİMLİ, SCHOTTKY FOTODİYOT ÜRETİMİ VE KARAKTERİZASYONU

Erhan Polatkan Ata
Fizik Doktora
Tez Yöneticisi: Doç. Dr. Ekmel Özbay
10 Temmuz 1998

Hızla gelişen "photonics" teknolojisi, diğer teknolojilerin vaadetmiş olduğundan daha yüksek bant genişlikleri vaadetmektedir. Artan iletişim, sadece bilim ve teknolojiyi geliştirmekle kalmayıp, aynı zamanda tarihteki en önemli devrimlerden birini, küresel kültür alışverişini sağlamaktadır.

Optolektroniğin yaşamsal elemanlarından olan fotodetektörler, artan iletişim talebini karşılayabilecek performanslara ulaşabilmek için hala geliştirilmektedir. 800-850 nm dalgaboyları için yüksek verimli ve yüksek hızlı, rezonant kavite ile güçlendirilmiş (RCE) Schottky fotodiyotlar tasarladık ve ürettik. Yüksek performans elde ettiğimiz GaAs/AlGaAs temelli iki ayrı yapı kullandık. Bu yapılardan birisinden verimlilikleri %50, 3-dB bant genişlikleri de 80 GHz olan fotodiyotlar ürettik. Öteki yapının tasarımı üretim öncesi dalgaboyu ve aktif katman kalınlık ayarı yapmaya uygun idi. Bu yapı üzerinde %20 kuvantum verimliliği ve RCE fotodiyotlar için dünya rekoru olan, 110 GHz öngörülen 3-dB bant genişliği elde ettik.

Aktif katmanın, yüzeydeki Au katmanının ve silikon nitrat katmanının

kalınlıklarının RCE aygıtlar üzerindeki etkilerini de inceledik. Aynı zamanda, teori ve deney arasındaki farklılıkları da kısaca açıkladık.

Fotodiyotların performanslarını arttırmaya yönelik teknikler, olası gelecek çalışması olarak önerdik. Ayrıca, konu ile ilgili edindiğimiz tecrübenin kullanılabileceği olası uygulamalara da değindik.

Anahtar Sözcükler: Rezonant Kavite, Rezonant Kavite İle Güçlendirilmiş, Fotodiyot, Schottky Eklemi, Kuvantum Verimliliği, Yüksek Hız.

Acknowledgements

It is my pleasure to express my deepest gratitude to my supervisor Ekmel Özbay for his invaluable guidance, motivation, morale support, and patience during my graduate study.

I wish to thank the past and present members of the physics department, without whom this study would not be possible. Especially, the members of Advanced Research Laboratories, who (somehow) managed to turn hard times into enjoyable ones.

I wish to address invaluable helps and hospitality of M. Selim Ünlü and his graduate students during my visit to Picosecond Laboratory at Photonics Center of Boston University.

I wish to thank the members of my proposal and Ph. D. defense committee, for their helpful guidance and constructive criticisms.

I am in debt to my family and friends for their supports and patience. Without them, I would not be who I am.

Savathanks for those who have made music for me, and reminded that "in the dark, it is easier to see."

The precious one who loves me and whom I love; you give me everything I need.

Contents

List of Figures

List of Tables

Chapter 1

Introduction

Light has always been an important medium of communication, even in prehistoric ages. An interesting example, from the historic ages of course, is the communication of the fall of Troy to Queen Clytemnestra in 1184 B. C., by a series of line of sight beacons of fires covering 900 km! Until scientists and researchers discovered light-material interactions (and vice versa), such as Nobel Prize awarded discovery of photo-electric effect by Albert Einstein, and developed methods to create, guide, and detect light; the only light sources, for communications, were heavenly bodies and fire. The guides were simple optical lenses and mirrors, and sensors were human eyes. The first two components, namely sources and guides, has always meant some level of technology, existed for centuries. The third, detection, has been performed by human eye until last few decades. Today, information systems use light without any need for a human eye, well, at least at some intermediate stages! This has been possible by developments in the fields of light generation (like lasers), transfer (like optical fibers), and detection (like photodetectors), "photonics" in short. In this work we studied some aspects of the light detection, photodetection, on a class of photodetectors, namely photodiodes.

Although the above paragraph is about optical communications, photodetectors find applications in many fields of science and technology, with an increasing rate and broadening range of applications. Photodiodes are vital

components of optoelectronic systems, which explains the importance of maturing their performances. Our work covers experimental study of a specific family of photodiodes, namely resonant cavity enhanced (RCE) Schottky photodiodes, supported by theoretical computer simulations.

1.1 Why Schottky Photodiodes?

Surprisingly, knowledge on Schottky contacts is maybe older than Schottky himself. More than a hundred years ago work of Braun in 1874,[1] showed the asymmetric nature of electrical conduction of metal contacts on semiconductors, such as copper on iron sulphide. First point contact detector patent was taken in 1906 by Pickard.[2] Although technologically oldest of semiconductor electronic components, the understanding of rectification mechanism took long decades of studies, both experimental and theoretical, of famous names, Schottky, Mott, Davydov, Bethe, Bardeen, Crowell, Sze, Mead, and many others. Even though working models and theories have been developed, a full physical understanding and prediction of Schottky contacts, especially on III-V materials, are still not as developed as for many of the other semiconductor devices. The reader is referred to the book by Rhoderick and Williams[3] for detailed information on metal-semiconductor junctions.

The advantages of Schottky diodes are their simplicity, easily obtainable compatibility with almost any microelectronics fabrication process, and excellent high speed performances. Schottky barrier diode being a majority carrier device, does not suffer from response delays arising from the minority carrier diffusion issues, which explains its multi-terahertz high-speed performance. As will be explained in section 2.3, speed limitations of a Schottky photodiode depends on carrier transit time and RC time constant, which can be kept small with ease compared to other types of photodiodes by a careful design of a Schottky device.

Applications in terahertz regime include mixers,[4,5] detectors,[6] and harmonic multipliers.[7] To our knowledge, first use of a metal-semiconductor diode as a high-efficiency photodetector is made by Ahlstrom et. al. and Schneider.[8,9] Since then,

3-dB bandwidths in excess of 100 GHz discrete[10,11] and monolithically integrated devices[12] have been reported.

1.2 Why Resonant Cavity Enhancement?

The modern society demands almost unlimited communication, which requires systems with extreme capacity performances. Optical fibers have telecommunication bandwidths about 25 THz, which is three orders of magnitude larger as compared to present optoelectronic systems with operating capacities less than 10 gigabits per second. Present microelectronics technology is not capable to increase bandwidth of electronic systems to such high values. However, similar to parallel processing in computers, we can use a larger fraction of the fiber capacity by means of parallel communication channels through optical fibers. The realization of parallel channels is possible by the technique known as wavelength division multiplexing (WDM), in which up to 500 different wavelength optical signals can be transmitted through a single fiber.

Resonant cavity enhanced (RCE) photodetectors have the advantages of both wavelength selectivity and high quantum efficiency, without any sacrifice of high speed performance.[13] Although fundamental physics of resonant cavities has been known for more than a hundred years, their implementation to optoelectronics became a hot topic in early 1990s.

Recent accomplishments by means of RCE effect can be summarized as follows. Avalanche photodetectors (APDs) with 75 % peak external quantum efficiencies,[14] low gain bandwidth of 33 GHz, and gain-bandwidth product of 290 GHz[15] were fabricated by a group at University of Texas at Austin. The same group made use of a 1 μm thick polysilicon absorption layer combined with Si-SiO_2 Bragg reflectors to obtain 44% quantum efficiency and bandwidth >1.4 GHz.[16] Intracavity resonant quantum well photodetectors embedded in vertical cavity surface emitting laser (VCSEL) structures were demonstrated at UC Berkeley. These detectors were intended as feedback devices for VCSELs fabricated and yielded the required low sensitivity to spontaneous emission and

high effective responsivity for the first time in such an application.[17] The same group also fabricated 30 nm wide and continuously tunable RCE photodetectors, that can also operate in wavelength tracking mode, a very attractive feature for robust WDM, spectroscopy, and wavelength applications.[18] In UC Santa Barbara, InGaAs/InAlGaAs/InP photodetector arrays for WDM applications with 4 nm channel spacing and a 17 GHz gain-bandwidth product for p-i-n photodetectors were realized.[19,20] InGaAs metal-semiconductor-metal (MSM) photodetectors with 10 GHz bandwidths and 77% external quantum efficiencies were fabricated at Technische Universitat Berlin.[21] RCE photodetectors operating at near 2 μm wavelength range with maximum quantum efficiencies of 85% were fabricated at Rutgers University.[22] A polarization sensing RCE photodiode structures were proposed from Boston University.[23]

1.3 RCE Schottky Photodiode Research

Several groups have demonstrated RCE Schottky photodiodes. The first RCE Schottky photodiode in the literature was reported by a group from AT&T Bell Laboratories, in 1990.[24] Their GaInAs based photodiodes had a relatively low, 1.5 fold, enhancement at 1.53 μm operation wavelength. Design and fabrication of a GaAs Schottky barrier photodiode with 9 GHz bandwidth and 80% quantum efficiency at 840 nm wavelength has been realized at University of Florida.[25] The UC Santa Barbara group[19] fabricated InGaAs based RCE Schottky photodiodes for comparing with similar p-i-n structures, but they did not mention any high speed and efficiency results for the Schottky photodiodes, but reported 21% efficient p-i-n structures. Though their high efficiency capabilities, wavelength selectivities, or tunability, among the aforementioned devices, only RCE Schottky photodiodes fabricated in our laboratories have shown high speed performance that first reached through 20 GHz bandwidth,[26] which later reached through 50 GHz[27] and 100 GHz[28] bandwidths for 800-850 nm and 900 nm wavelength operations, respectively.

As a part of this work, we aimed to increase the gain-bandwidth product of

RCE Schottky photodiodes. For this purpose we fabricated various photodiodes for 800-850 nm wavelength operation. Experimental and theoretical analyses have shown that, pulse responses of the fabricated devices were experimental setup limited. Bandwidth estimated to be over 110 GHz is reported. To our knowledge, this corresponds to fastest RCE photodetectors published in scientific literature.

Chapter 2

Theory

A photodiode is a solid-state sensor that detects optical signals through electronic processes. Basic electronic processes are: carrier generation with incident radiation, carrier transport and/or multiplication by means of a current-gain mechanism, and external circuitry to obtain a meaningful electrical output. Among various fields where photodetectors find applications, fiber-optic communications (800-1600 nm) field is the largest commercial market. As telecommunication became a part of our lives, communication speed and reliability issues became more important than ever. In the following sections, basic principles of photodetection are outlined. We then introduce a newly developed technique, namely resonant cavity enhancement (RCE), which can be used to increase detector speed and performance.

2.1 The Photodiode

A photodiode has a free charge carrier depleted semiconductor region with a high field. Photocarriers generated in the depletion region are collected through terminals of the device by means of the existing high field. In this work only Schottky barrier type photodiodes are fabricated, but the ideas developed can also be extended to other type of devices (p-n junction, p-i-n, MSM). Quantum efficiency, η, is perhaps the most fundamental property, as it determines just

how efficiently the device converts incoming photons into conduction electrons. Sometimes expressed in percentage, quantum efficiency is defined as number of electron-hole pairs per incident photon;

$$\eta = \frac{I_p/q}{P_{opt}/h\nu} \tag{2.1}$$

where I_p is the photo-generated current by the absorption of incident optical power P_{opt} at the wavelength λ (corresponding to a photon energy $h\nu$). Another related figure of merit is the responsivity, which is defined as the ratio of the photocurrent to the optical power;

$$R = \frac{I_p}{P_{opt}} = \frac{\eta\lambda}{h\nu} = \frac{\eta\lambda}{1.24}(A/W). \tag{2.2}$$

2.2 Metal-Semiconductor Photodiode

Figure 2.1 shows a typical energy-band diagram of a metal-semiconductor (Schottky) junction. For photodiode applications, the metal deposited is very thin (around 10 nm) to obtain semi-transparency for top illumination. There are three possible modes of operation;

1. For $E_g > h\nu > q\phi_b$ and $V < V_B$, where V_B is the avalanche breakdown voltage, photo excited electrons in the metal can overcome the barrier potential and can be collected through the semiconductor. This process can be used to determine Schottky-barrier height and to study hot-electron transport.

2. For $h\nu > E_g$ and $V < V_B$, the radiation produces electron-hole pairs in the semiconductor. Our diodes are normally operated in this mode, so this mode is discussed below.

3. For $h\nu > E_g$ and $V > V_B$, the diode can be operated in the avalanche breakdown region. The avalanche multiplication gives rise to internal current gain, which results in high quantum efficiencies. The disadvantage of this mode is relatively higher electrical noise as compared to normal operation.

Depletion layer width, W, due to the built-in and bias potentials is given as[29];

$$W = \sqrt{\frac{2\epsilon_s(V_{bi} - V - kT/q)}{qN_d}} \tag{2.3}$$

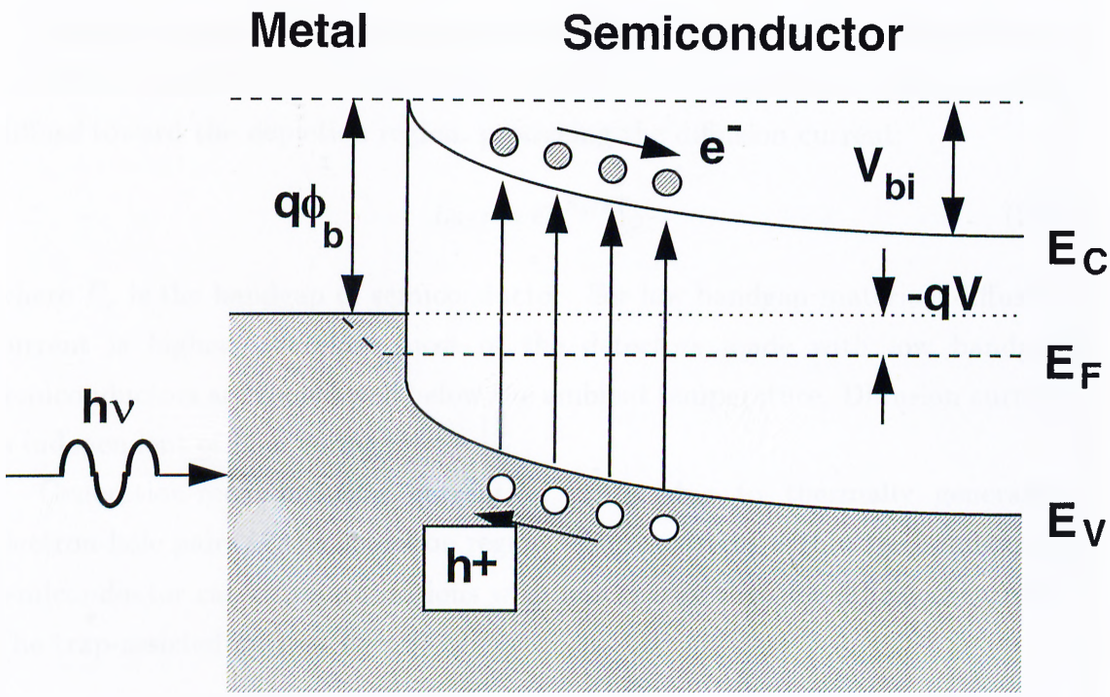

Figure 2.1: A schematic diagram of an illuminated Schottky junction.

where ϵ_s is the semiconductor dielectric constant, V_{bi} is the built-in potential, N_d is the impurity concentration of the semiconductor. Here it must be noted that, the capacitance of the junction is inversely proportional to the depletion width;

$$C = \frac{\epsilon_s A}{W} \tag{2.4}$$

where A is the area of junction. So the detector bandwidth increases with increasing depletion width, since bandwidth is defined as;

$$B = \frac{1}{2\pi RC} \tag{2.5}$$

where R is the sum of detector series resistance and load resistance.

A good photodetector should have high sensitivity and low noise. These characteristics are mainly determined by the dark current in the device. There are three main components of dark current: diffusion, generation-recombination, and tunneling currents.

Diffusion current, I_{diff}, is due to the thermally generated electron-hole pairs in the undepleted region of the semiconductor. Once produced, these carriers diffuse toward the depletion region, producing the diffusion current;

$$I_{diff} \propto e^{-E_g/kT} \tag{2.6}$$

where E_g is the bandgap of semiconductor. For low bandgap materials diffusion current is higher, therefore most of the detectors made with low bandgap semiconductors are cooled well below the ambient temperature. Diffusion current is independent of bias voltage.

Generation-recombination current, I_{g-r}, is due to thermally generated electron-hole pairs in the depletion region. Traps existent within the bandgap of semiconductor can cause excitations with less energy than for diffusion current. The trap-assisted current is[29];

$$I_{g-r} \propto (V_{bi} - v)^{1/2}\, e^{-E_g/2kT}. \tag{2.7}$$

From equation 2.3;

$$I_{g-r} \propto W e^{-E_g/2kT} \tag{2.8}$$

which tells us that generation-recombination current is proportional to the volume of depletion region, and differs from diffusion current by its reverse-bias dependence. For large bandgap materials, generation-recombination current usually dominates over diffusion current.

Tunneling (or field emission, FE) current is observed when there exist high field regions along the semiconductor. Under high field the geometrical width of the Schottky barrier decreases, producing a tunneling current. Similarly thermionic field emission (TFE) is the current due to the electrons excited to higher energy levels in the conduction band. For these high energy electrons, the Schottky barrier is thinner as compared to lower energy electrons. At room temperature both FE and TFE currents may be important for high levels of doping.[3]

2.3 Carrier Transport and Speed Limitations

High speed performance of a photodetector depends on several factors. Major factors are carrier transit time and RC time constant. Diffusion current, carrier trapping at the heterojunctions, and packaging/probing are also effective in determining high speed response. In the following pages these are discussed briefly, more detailed information can be found in references.[29-31]

Incident photons will generate electron-hole pairs in the active region of the detector. These carriers will travel across the depletion region by the forces exerted by built-in and/or the bias potentials. Figure 2.2 (a) shows a Schottky photodiode with a photo-generated electron-hole charge sheet of density σ. The electrons will drift to the ohmic contact on the right and the hole to the Schottky contact on the left. This transport produces a displacement current and reduces the internal electric field (Figure 2.2 (b), (c)). From Gauss's law the difference in electric field at the position of electron or hole is;

$$\Delta E = \frac{q\sigma}{\epsilon_s}. \tag{2.9}$$

Since the total voltage across the depletion region is constant, the reduced electric field between the electron and hole will be compensated by the increasing electric field outside. The rate of change of electric field at the position $X = X_1$ is;

$$\frac{\partial E}{\partial t} = -\frac{(v_e + v_h)\,\Delta E}{W} \tag{2.10}$$

where v_e and v_h are the saturated hole and electron velocities, respectively. Hence, the displacement current is given by;

$$i(t) = -\epsilon_s A \frac{\partial E}{\partial t} = q\sigma \frac{A}{W}(v_e + v_h). \tag{2.11}$$

The electron and hole currents last for time duration of $t_n = (W - X_o)/v_e$ and $t_p = X_0/v_h$, respectively (Figure 2.3 (a)). The total electron and hole currents are given by (see Figure 2.3 (b));

$$i_e(t) = \frac{qv_e A}{W} \int_0^W n(x,t)dx \tag{2.12}$$

$$i_p(t) = \frac{qv_hA}{W}\int_0^W p(x,t)dx \tag{2.13}$$

where $n(x,t)$ and $p(x,t)$ are electron and hole densities in the depletion region, respectively. The total current is the sum of these currents. Here, it must be noted that the current output waveform due to fast carriers (electrons in our case) has a lower duration than that of slower carriers (holes), so photo-carrier generation closer to the Schottky contact is advantageous.[32]

2.4 RC time constant

The simplified small signal circuit model of a Schottky photodiode is given in Figure 2.4. The junction capacitance, C_j, is the Schottky capacitance defined earlier. Series resistance, R_s, is the total resistance of junctions and bulk resistance. Parasitic capacitance, C_p, depends on geometry of the device and other external connections.

When external load of resistance R_L is connected to the diode, 3 dB bandwidth is;

$$f_{RC} = \frac{1}{2\pi\left(C_j + C_p\right)\left(R_L + R_s\right)}. \tag{2.14}$$

Hence one must be careful in the design to minimize parasitic resistance and capacitance. While characterizing high-speed response, the effect of R_L and C_p must be taken into account.

2.5 Pulse response

If a photodiode is uniformly illuminated, as the case in Figure 2.3, the time domain pulse response of the photodiode is the sum of two right-triangular components. Then, the corresponding transit-time limited frequency response of the photodiode is a combination of $sinc^2$ functions[20];

$$10\log\left|\frac{i^2(\omega)}{i^2(0)}\right| = -10\log\left(1+\frac{f^2}{f_{RC}^2}\right) + 20\log\left(\frac{1}{2}sinc^2\left(\pi f t_n\right) + \frac{1}{2}sinc^2\left(\pi f t_p\right)\right). \tag{2.15}$$

2.6 Diffusion current

When a significant absorption outside the high field regions exists, diffusion current may be important. Carriers within about one diffusion length will have a chance to diffuse into the active region, resulting in a tail in time domain response of the photodiode. At the edge of the depletion region, the electron diffusion current is[29];

$$J_e = qD_e \frac{\partial n}{\partial x} = qD_e \frac{\Delta n}{L_e} \tag{2.16}$$

and hole diffusion current is;

$$J_h = -qD_h \frac{\partial p}{\partial x} = qD_h \frac{\Delta p}{L_h} \tag{2.17}$$

where $D_e(D_h)$ is diffusion coefficient and $L_e(L_h)$ is diffusion length for electrons (holes). With a photo carrier density equal to n the electron diffusion current is;

$$J_{diff} = qn\mu_e \left(\frac{kT/q}{L_e} \right) \tag{2.18}$$

and is a relatively slow process compared to the drift process;

$$J_{drift} = qn\mu_e E \tag{2.19}$$

where μ_e is the electron mobility and E is the electric field. For most of the devices, the electric field along the depletion region is much greater than $(kT/q)/L$. However, for high speed detectors, extra care may be required to eliminate the diffusion tail.

2.7 Carrier Trapping

When there exist conduction (valance) band discontinuities, electrons (holes) are trapped at these discontinuities. The associated emission rate may be approximated by thermionic emission, which is related to the Schottky (like) barrier height due to band discontinuity ϕ_{bc}, through the relation;

$$\frac{1}{\tau_e} = Be^{-\phi_{bc}/kT} \tag{2.20}$$

where τ_e is emission time constant for electron, B is a constant, and ϕ_{bc} is the barrier height for the conduction band. Similar equations hold for holes as well. As the applied bias decreases barrier height, trapping will decrease. For reducing the trapping effect, superlattice or compositional grading may be introduced at the heterointerfaces.[33] In our designs, carrier trapping is reduced by the latter method.

2.8 Quantum Efficiency of a Metal-Semiconductor Photodiode

Calculation of quantum efficiency of a photodiode requires calculation of photocurrent under known illumination. For a simple calculation we can introduce some assumptions. For high speed detectors the absorption length is small, $\alpha L \ll 1$. As long as energy bandgap is not small for a moderately doped absorbing layer, thermal generation current can be neglected. Absorption in the metal and other layers can also be neglected. Under these assumptions, we can proceed as follows. The hole electron generation rate is;

$$G(x) = \Phi_0 \alpha e^{-\alpha x} \tag{2.21}$$

Φ_0 is the incident photon flux per unit area, which is given by;

$$\Phi_0 = \frac{P_{opt}(1-R)}{Ah\nu} \tag{2.22}$$

where R is the reflection coefficient and A is the device area. The drift current is found by integrating $G(x)$ over the depletion region (see Eqn. 2.16 and 2.17). Thus we have an expression for current (neglecting diffusion current);

$$J_{tot} = q\Phi_0 \left(1 - e^{-\alpha L}\right) \tag{2.23}$$

which yields an expression for the quantum efficiency of a conventional photodiode;

$$\eta = (1-R)\left(1 - e^{-\alpha L}\right) \simeq (1-R)\alpha L \tag{2.24}$$

Now, consider a photon flux density given by $\Phi_1 e^{j\omega t}$, then the conduction current at depth x from the surface is;

$$J_{cond}(x) = q\Phi_1 e^{j\omega(t-x/v_s)} \tag{2.25}$$

where saturation velocity v_s for carriers is assumed. Integrating throughout the depletion region yields the short circuit current (the displacement current due to built-in and any applied potentials, which sum up to zero, is zero) is;

$$J_{sc}(x) = \frac{q\Phi_1 (1 - e^{j\omega\tau})}{j\omega\tau} \tag{2.26}$$

At $\omega\tau = 2.4$, the current amplitude is reduced by $\sqrt{2}$. Hence, the 3 dB frequency is given by;

$$f_{3dB} = \frac{2.45}{2\pi\tau} \simeq \frac{0.45v_s}{L} \approx 0.45\alpha v_s \tag{2.27}$$

Here it must be noted that, for these calculations, one must use transit time (τ) of the slower carriers, usually the holes. The bandwidth efficiency product is;

$$f_{3dB}\eta \approx 0.45\alpha v_s(1 - R) \tag{2.28}$$

and is independent of design parameters.[35] This analysis shows the trade off between quantum efficiency and bandwidth of a photodiode. However, the resonant cavity enhancement technique, described in the subsequent section, overcomes this trade off.

2.9 Resonant Cavity Enhancement

For high speed operation, the depletion region must be kept thin in order to have a small carrier transit time. On the other hand, for high efficiency (electrical output versus optical input) it must be sufficiently thick to absorb a high fraction of incident radiation. This trade off between the response speed and efficiency can be overcome by means of RCE method. In this technique absorbing layer

is kept thin, resulting in a low transit time, on the other hand incident light is trapped in a Fabry-Perot cavity so that light absorption is high.

Principals of resonant cavity enhancement (RCE) depend on placing active layer of the device inside a Fabry-Perot resonant microcavity. The enhanced optical field in the cavity enables thinner active layer without sacrificing quantum efficiency. Since the speed of light is about three orders of magnitude higher than that of carriers, there exists a non-significant pulse broadening. A schematic diagram of a resonant photodetector is given in Figure 2.5 where; E_x $(x = i, f, b)$ is the electric field, α_{ex} is the absorption coefficient outside the active region, and t_1 is the transmission coefficient, and $r_i e^{-j\varphi_i}$ $(i = 1, 2)$ denotes reflection coefficients of top and bottom mirrors with their phases. The forward traveling wave at $z = 0$ (with propagation constant β) can be calculated as[13];

$$E_f = \frac{t_1}{1 - r_1 r_2 e^{-\alpha d - \alpha_{ex}(L_1+L_2)} e^{-j(2\beta L + \varphi_1 + \varphi_2)}} \cdot E_i \tag{2.29}$$

thus the backward traveling wave is;

$$E_b = r_2 e^{-\frac{\alpha d}{2}} e^{-\frac{\alpha_{ex}}{2}(L_1+L_2)} e^{-j(\beta L + \varphi_2)} E_f. \tag{2.30}$$

The optical power inside the cavity is;

$$P_s = \frac{n}{2\eta_0} |E_s|^2 \quad (s = f, b) \tag{2.31}$$

where η_0 and n are the vacuum characteristic impedance and the refractive index of the detector material, respectively. Optical power absorbed in the active layer (neglecting the standing wave effect discussed in the following paragraphs) is;

$$P_1 = \frac{(1 - r_1^2)\left(e^{-\alpha_{ex}L_1} + r_2^2 e^{-\alpha_{ex}L_2 - \alpha_c L}\right)\left(1 - e^{-\alpha d}\right)}{1 - 2r_1 r_2 e^{-\alpha_c L}\cos(2\beta L + \varphi_1 + \varphi_2) + (r_1 r_2)^2 e^{-2\alpha_c L}} \cdot P_i \tag{2.32}$$

Quantum efficiency η, is the ratio of the absorbed power to the incident optical power (assuming all the photo-generated carriers are collected at the device terminals) and hence;

$$\eta = \frac{\left(e^{-\alpha_{ex}L_1} + R_2 e^{-\alpha_{ex}L_2} e^{\alpha_c L}\right)}{1 - 2\sqrt{R_1 R_2} e^{-\alpha_c L}\cos(2\beta L + \varphi_1 + \varphi_2) + R_1 R_2 e^{-\alpha_c L}} (1 - R_1)\left(1 - e^{-\alpha d}\right) \tag{2.33}$$

where $R_i = r_i^2$ $(i = 1, 2)$ and α_c is given by;

$$\alpha_c = \frac{\alpha_{ex} L_1 + \alpha_{ex} L_2 + \alpha d}{L} \tag{2.34}$$

In most cases, the absorption coefficients of materials around the active layer are small (α_{ex}~ 5-10 cm^{-1}) compared to the active layer ($\alpha \geq 10^4$ cm^{-1}), thus if active layer is not extremely thin compared to its surrounding materials, α_{ex} can be neglected and quantum efficiency expression can be simplified as;

$$\eta = \frac{1 + R_2 e^{-\alpha d}}{1 - 2\sqrt{R_1 R_2} e^{-\alpha d} \cos(2\beta L + \varphi_1 + \varphi_2) + R_1 R_2 e^{-\alpha L}} (1 - R_1)\left(1 - e^{-\alpha d}\right). \tag{2.35}$$

Here the term in braces is the enhancement factor, which becomes unity if $R_2 = 0$ and η becomes that of a conventional photodiode. Another important feature of resonant detection must be noted; η is a periodic function of the inverse wavelength ($\beta = 2n\pi/\lambda_0$) and is enhanced periodically at the resonance wavelengths satisfying the condition $2\beta L + \varphi_1 + \varphi_2 = 2m\pi$ $(m = 1, 2, 3, ...)$.

In Figure 2.6, wavelength dependence of quantum efficiency, for the RCE structure in Figure 2.5, is plotted for various top mirror reflectivities ($R1$=0.05,0.3,0.9). For comparison, quantum efficiency $(1 - e^{-\alpha d})$ of a conventional photodetector (same structure without top and bottom reflectors) is also plotted on the same graph. Fixed parameters were chosen as $R_2 = 0.9$, $L = 2m$, $\alpha_d = 0.1$, $\beta = 2n\pi/\lambda$, $n = 3.6$, and $\varphi_1 = \varphi_2 = 0$.

The peak η at the resonance wavelength can be calculated by inserting this resonance condition in the above equation;

$$\eta_{\max} = \frac{1 + R_2 e^{-\alpha d}}{\left(1 - \sqrt{R_1 R_2} e^{-\alpha d}\right)^2} (1 - R_1)\left(1 - e^{-\alpha d}\right). \tag{2.36}$$

With proper design quantum efficiencies near unity are possible.

The spatial distribution of the optical field inside the cavity is altered by the so called standing wave effect (SWE). The back and forth propagating fields create a standing field distribution inside the cavity, which means that η is a function of the spatial position of absorbing layer in this field, unless it is so thick

to span several periods of the standing wave. The SWE is introduced into η by defining $\alpha_{eff} = SWE \cdot \alpha$, which may enhance or decrease η depending on position. Calculation of SWE requires perturbation analysis of Maxwell's equations, and if required some assumptions such as negligible absorption outside active region, uniform absorption in active layer. With these simplifications, an expression for SWE, in terms of the cavity parameters is[13];

$$SWE = \frac{\alpha_{eff}}{\alpha} = 1 + \frac{2r_2}{\beta d\,(1 + r_2^2)} \sin(\beta d) \cos(2\beta L_2 + \beta d + \varphi_2)\,. \tag{2.37}$$

The SWE depends explicitly on back mirror reflectivity (r_2, φ_2), and implicitly (through the resonance condition, $2\beta L + \varphi_1 + \varphi_2 = 2m\pi$) on top mirror phase (φ_1). Dependence on λ is both explicit through β, and implicit through strong wavelength dependence of complex mirror reflectivities. Knowledge and control of the phase behavior are especially important for the positioning of the thin active layers. In general, computer simulations making use of scattering matrix (S-matrix), transmission line, or propagation matrix theories, are used to calculate and design proper photodiodes. Our structures were designed by using S-matrix formalism.[34]

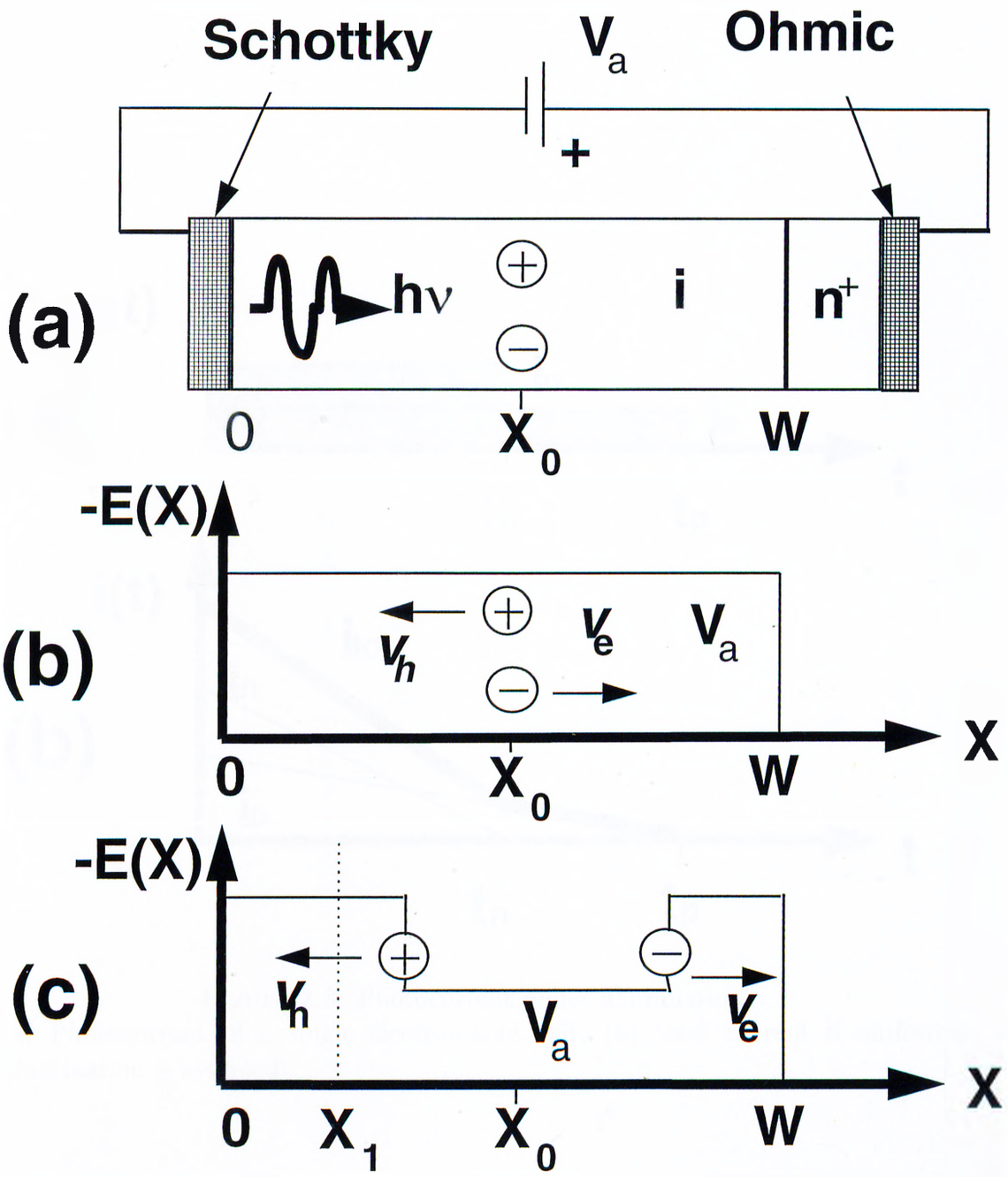

Figure 2.2: Biased Schottky photodiode and electric field distributions (a) Biased Schottky photodiode, (b) electric field distribution at the time electron hole pairs are generated, (c) the resultant electric field distribution after electron-hole pairs are separated.

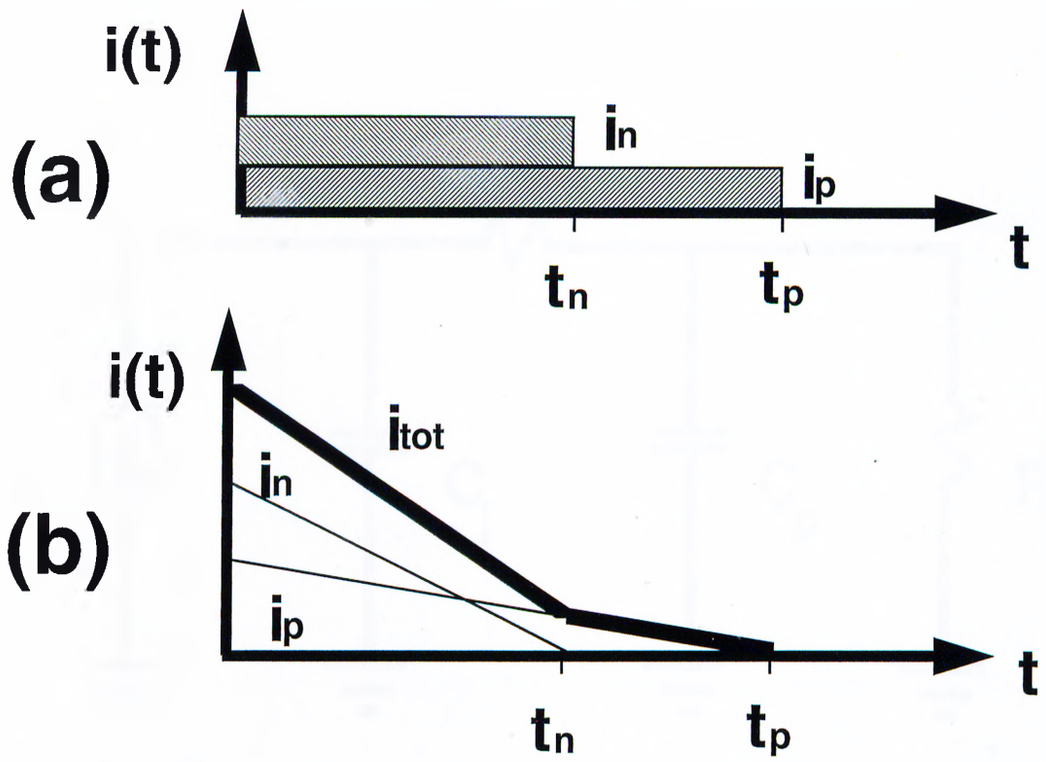

Figure 2.3: Photocurrent under illumination.
(a) Photocurrent of a single electron-hole pair, (b) total current if uniform illumination is assumed.

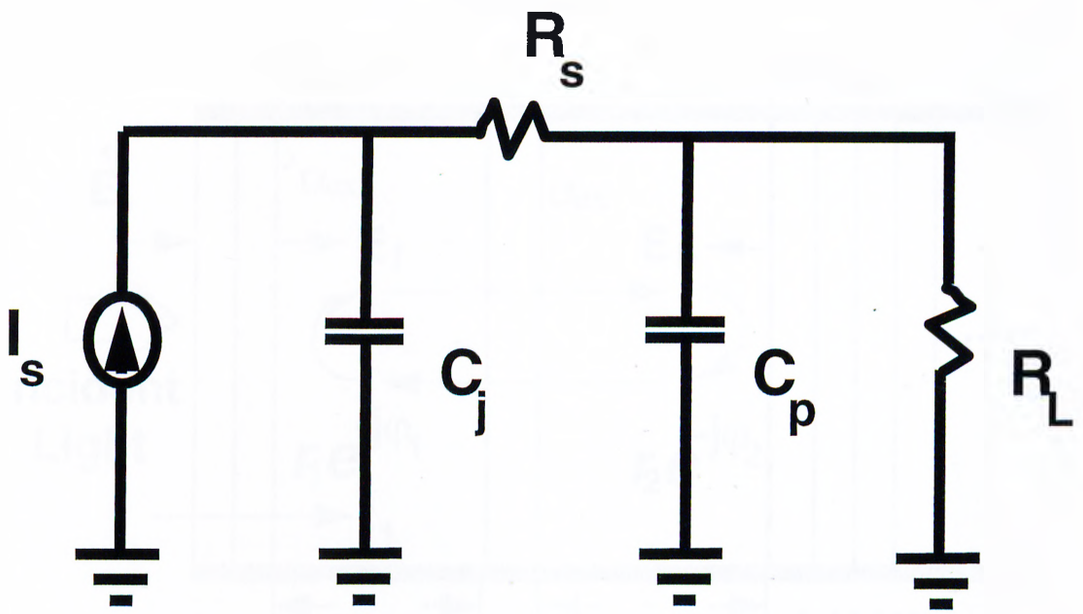

Figure 2.4: Simplified equivalent circuit of a Schottky photodiode.

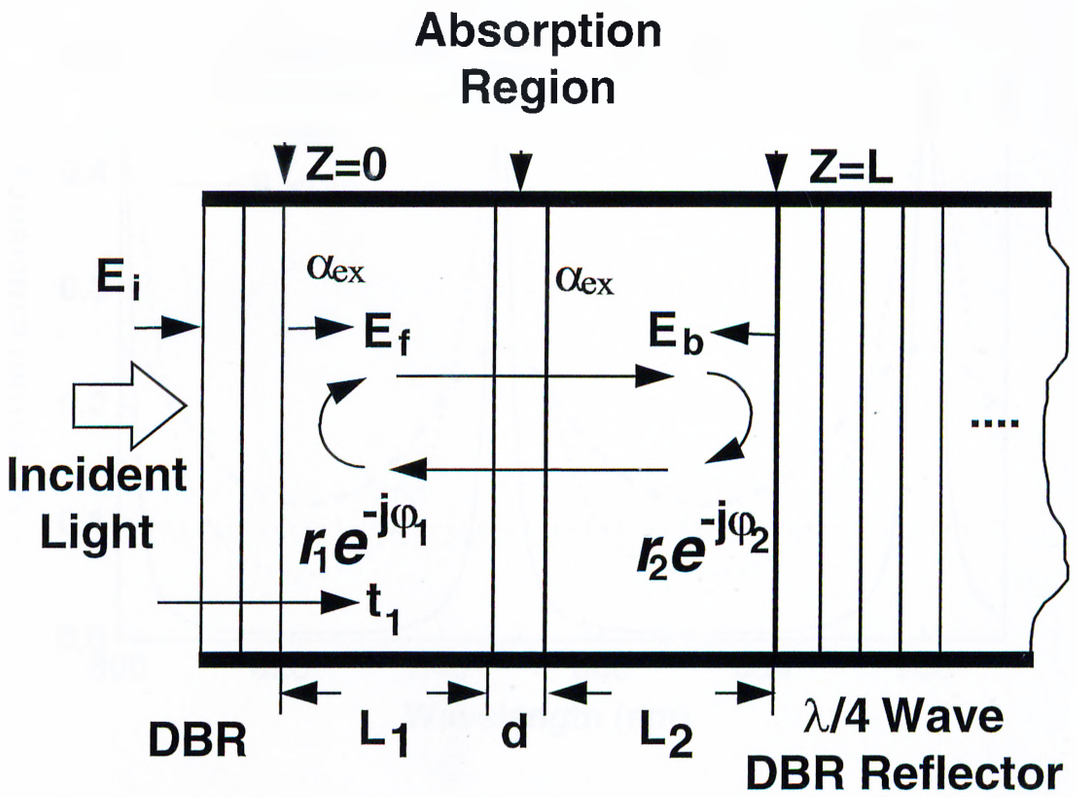

Figure 2.5: Schematic diagram illustrating RCE effect.

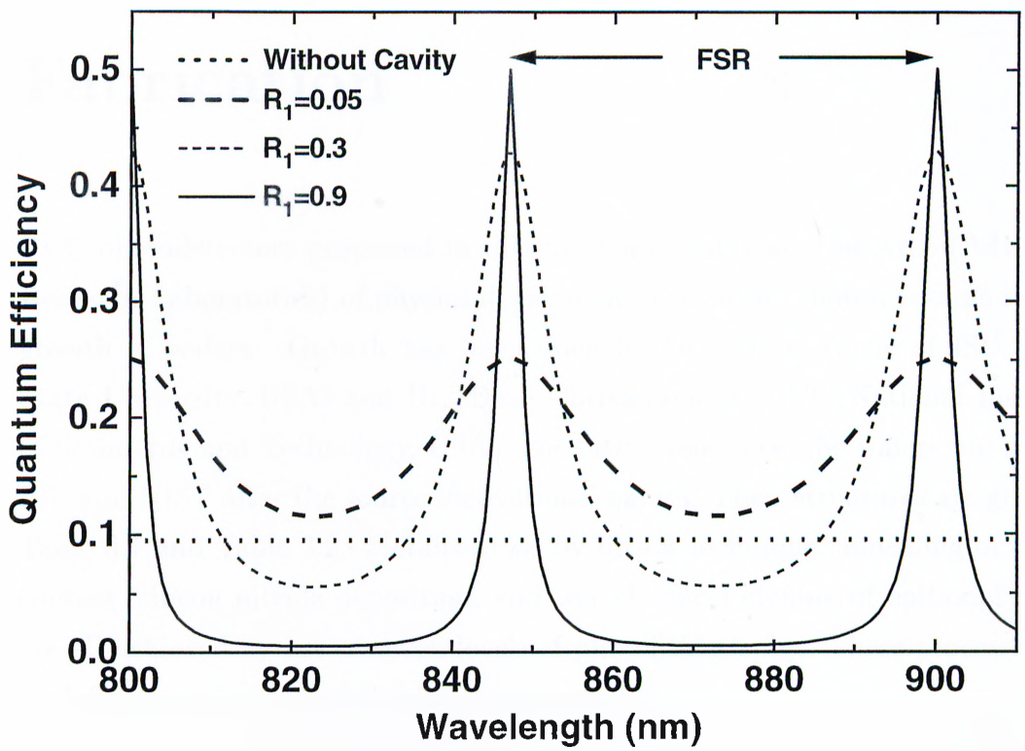

Figure 2.6: Wavelength dependence of quantum efficiency.
For fixed absorption thickness, fixed bottom mirror reflectivity, and varying top mirror reflectivity.

Chapter 3

Fabrication

RCE photodetectors processed in this work were fabricated in ARL (Advanced Research Laboratories) of physics department, except for photomasks and MBE growth of wafers. Growth has been done by Dr. Gary Tuttle of ISU (Iowa State University, USA) and Dr. Dave Christensen of NIST (National Institute of Standards and Technology, USA). For future reference, the wafers are named ISU and NIST after the source institutions' names. Their structures are given in Table 3.1 and Table 3.2. Metalizations by lift-off technique, annealing of ohmic contact, silicon nitride deposition, and wet chemical etching of epitaxial layers are all achieved by use of seven levels of photolithography. These processes are explained briefly in the following paragraphs.

3.1 Sample Preparation and Cleaning

Processing starts with cleaving the crystal, to obtain a piece that is large enough to handle and small enough for economic use of the original crystal. Dimensions for our samples vary between, approximately, 6×6-10×10 mm. The cleanliness of the sample, materials used (metals, chemicals, etc.), environment, and the masks are critical for the success of the fabrication. Dirt in an early process step may result in larger dirt or defects as the forthcoming processes are carried out. The formula for yield Y of a process, with the assumption that the defects are

Material	**Doping (cm^3)**	**Thickness (nm)**
$Al_{0.15}Ga_{0.85}As$	10^{17}	80
$Al_{0.15}Ga_{0.85}As \rightarrow GaAs$	10^{17}	30
GaAs	10^{17}	120
$GaAs \rightarrow Al_{0.20}Ga_{0.80}As$	10^{17}	30
$Al_{0.20}Ga_{0.80}As$	10^{17}	160
$Al_{0.20}Ga_{0.80}As$	n^+	400
$Al_{0.20}Ga_{0.80}As$	undoped	230
$Al_{0.20}Ga_{0.80}As$	10^{17}	160
Bragg Mirror (18.5 pairs)		
Semi-insulating GaAs Substrate		

Table 3.1: Structure of the NIST sample

Material	**Doping (cm^3)**	**Thickness (nm)**
GaAs	3×10^{16}	330
$GaAs \rightarrow Al_{0.20}Ga_{0.80}As$	10^{18}	50
$Al_{0.20}Ga_{0.80}As$	$n^+ = 10^{18}$	500
$Al_{0.20}Ga_{0.80}As$	undoped	260
Bragg Mirror (14.5 pairs)		
Semi-insulating GaAs Substrate		

Table 3.2: Structure of the ISU sample

uniformly distributed, is[36];

$$Y = e^{-DA_c} \tag{3.1}$$

where D is the defect density and A_c is the critical or active area of the sample in process. The critical area is the area of the devices that when a defect exists in this area, device will not work appropriately.

Let us investigate the effect of dust particles for example. Our processes are carried out in a class 100 room, which means that number of particles with diameters larger than 1 μm are limited by 100 in a cubic foot volume. Assuming a 3.6 km/h(1m/s) air flow, number of particles hitting on per square foot is approximately 300, which corresponds to 0.2 particles/(minute $\times$ mm^2). Our dice (process) area is approximately 5×5 mm^2, which means that dust-like particles impinging on our active process area are limited by one, for every two minutes.

Unless we leave our sample uncovered for long periods, dust is a big problem of VLSI producers, not ours!

However, we still have other contamination problems, mainly photoresist residuals, films produced by chemical processes. These problems can be reduced by means of wet chemical techniques called three solvent cleaning (TSC). TSC must be done before almost every photolithography step to achieve a high yield. Simply; TSC is immersing sample in (hot) threechlorethylene (TCE), then in acetone, and then in (hot) isopropyl alcohol (ISO) for short durations (2-10 minutes in each). TCE mainly dissolves any possible oils, acetone dissolves organic molecules such as photoresist residues and TCE, and ISO dissolves acetone. After ISO, sample is rinsed in deionized water (DI) and blown dry by a nitrogen gun and then dehydrated (to get rid of possible humidity on surface) on a hotplate set at 110 or 120° C for 1-2 minutes, which finishes the TSC process.

3.2 Photolithography

Photolithography is the most frequent process step. In each step of fabrication micro-geometry must be defined on the samples, which is done by lithography. Lithography is similar to making a black and white photo from the negative film. We are using a liquid photoreactive chemical, namely photoresist, to create an image of our negative (photomask) on the wafer. The liquid is spun on the sample and prebaked (on a hotplate) for obtaining a nonsticking photoreactive film. This film is exposed (to UV-light) through a photomask, and then developed in a solvent that removes the UV-exposed part (for the, so called, negative photoresist the unexposed parts are developed) leaving us a patterned film. This film is mechanically and chemically robust enough that we can deposit metals on it or etch through it.

For photolithography steps other than thick (close to 1μm), photoresist is prebaked on hot plate at 110° C for 1 minute. Before wet chemical etches, the resist is post baked on hot plate at 110-120° C for 1 minute. The airbridge level is a process developed by Saiful Islam[37] of our laboratory, which

requires a photolithographic airbridge post level that completely differs from other lithography levels. The developed photoresist of this level must remain undistorted until air bridges are completed. Therefore this photoresist is very hard baked in oven at 140° C for 30 minutes, and thinned by RIE (reactive ion etcher).

3.2.1 Image-reversal technique

The thickness of the photoresist depends on spin rate and bake conditions. These parameters are varied during our processes. For thick material depositions (interconnect and airbridge levels) the resist was spun at relatively low speeds (2500-3000 rpm) and then soft baked in oven (80° C, 30 minutes). These resulted in a thick photoresist with a harder, than core, resist surface. The surface was further hardened by immersing the sample in chlorobenzene for 15 minutes. Harder resist meant, harder to develop, so surface was developed slower than underlying core and we had over hanging resist edges, which had improved the lift-off process explained below.

However, we have encountered poor quality interconnect metalization problems. The lift-off yield was low especially for air-bridges. To improve yield and quality we decided to introduce the "image-reversal" technique into our photolithography steps. The photo resist (AZ 5214E) used in our all lithography processes allows to "reverse" the image exposed from positive to negative. This reversal automatically results in an undercut edge suitable for lift-off process. This reversal is accomplished by chemically changing the photochemically generated acid into an inhibitor. After an exposure similar to standard exposures a post-exposure bake makes exposed areas insoluble by cross linking the polymer based photoresist.[36] Normally, the exposure is larger near the top of any resist, which results in a more rapid development near the surface and yields a resist profile with positive slope, for positive resists. However, after image reversal this profile is also reversed, resulting in an undercut profile. A flood exposure after the post-bake is usually used to enhance the development

selectivity between exposed and unexposed regions.

Actual process developed in our laboratory is as follows. Standard spin and prebake for thick resist (3000-4000 rpm, 110^o C for 1 minute on hot plate) is carried out. Following exposure, post-bake at 115^o C for 2 minutes is performed on hot plate. A flood exposure (*i.e.*, without any mask) is followed by standard development. For this reversal lithography step, negative masks must be designed by taking into account the reversals in alignment marks, *etc.* In Figures 3.1 and 3.2 SEM photos taken during image-reversal technique development are seen. In both samples seen in these photos, gold is deposited everywhere on sample surface, except near the photoresist edges where undercut edge profile resulted in shadowing. Gold (which looks like snow in the photos) also makes an undercut edge similar to snow accumulation on sharp edged objects.

3.3 Metalization

It is very hard to think electronic devices without metals. In our fabrication we have used lift-off metalization technique to make ohmic and Schottky contacts, and interconnection between them. Lift-off is a common technique of metalization. After the required metalization layout is defined by photoresist (by lithography), the samples are coated by required materials. Since the resist film has a finite thickness, the coated material (if thin enough) will be discontinuous at the pattern edges of the resist. Thus, when immersed in acetone the photoresist will be dissolved "lifting-off" the material on it, and we are left with a patterned material on the surface of sample. As mentioned earlier, before thick material depositions, the appropriate modifications were introduced to photolithography. The ohmic and Schottky level lift-offs are easier since; in ohmic level samples are etched down to a depth comparable to metalization thickness and Schottky metal is very thin ($\sim$ 10 nm). If samples in Figures 3.1 and 3.2 are immersed in acetone, the resist will be dissolved and the gold on top of the resist patterns will float away from the sample. We will be left with line shaped and circular holes in gold for samples in Figures 3.1 and 3.2, respectively.

3.4 Wet Chemical Etching

Our processes are not of planar type, that is, we have to etch through the wafer surface. First, we must make contacts to an epitaxial layer buried under the surface of wafer, second we must isolate devices by making mesas, third we must make contacts to metalizations beneath the silicon nitride. For all of these purposes we use wet (aqueous solution of) chemical etchants. For $Al_xGa_{1-x}As$ materials we prefer an etchant based on ammonia, which is ammonium hydroxide: hydrogen peroxide: water (14:2.4:200 volume ratio) solution. For silicon nitride etching, hydrofluoric acid: water (1:100 volume ratio) solution is used. Before etching the patterned photoresist is postbaked to obtain a better adhesion on the wafer surface. An oxygen plasma ash cleaning of the surface is preferable prior to etching. The etch depth (ratio) is determined with a surface profilometer (DEKTAK 3030) to stop the etch at a required depth.

3.5 Dielectric Coating

In our processes, a dielectric layer (silicon nitride, Si_3N_4) is used for two purposes. It serves both as a dielectric for bias capacitors of our circuits and a surface dielectric mirror to enhance resonant cavity effect. The dielectric deposition is done by a technique known as PECVD (plasma enhanced chemical vapor deposition), in which the growth temperature can be kept lower compared to other techniques such as CVD. The plasma generated in the system is able to generate chemically reactive molecules at relatively lower temperatures because of the non-equilibrium nature of the plasma state. The temperature of the environment is relatively low, 250° C for our processes, while electrons can exhibit tens of thousands of degrees Kelvin. Thus we can obtain film growth at low temperatures, which otherwise would require more than 700° C temperatures, damaging previous processes. We have used silane (SiH_4) as the source of Si, and ammonia (NH_3) as the source of N. The expected reaction is[36];

$$3SiH_4 + 4NH_3 \rightarrow Si_3N_4 + 12H_2 \tag{3.2}$$

but there are an enormous number of possible intermediate reactions, which are beyond the scope of this thesis. Further information on this subject can be found in the literature.[38]

3.6 Photodiode Fabrication Process

The wafers are cleaved to appropriate dimensions, and cleaned by TSC. ISU sample is etched for wavelength tuning before the process, this procedure will be explained in measurements chapter. After the ohmic contact patterns are defined by lithography, we etch the NIST and ISU samples down to 600-650 nm depth to reach n^+ GaAs layer. Then Ge/Au/Ge/Au (10.8/10.2/6.3/23.6 nm) and Ni/Au (10/550-600 nm) are defined by lift-off technique. The Au thickness (~ 600 nm), following Ni, is chosen to have an almost planar surface. Then the samples are annealed in RTP (rapid thermal processor) at 425^o C for 30 seconds to achieve good quality ohmic contacts. This process results in Ge diffusion into the GaAs, resulting in a highly degenerate GaAs surface. Photomasks of the forthcoming levels are aligned to this ohmic level. The next step is isolating the devices by wet etching down to undoped region on top of Bragg reflectors. Depositions of an interconnect Ti/Au (10-15/1000 nm) metal and a Au (10 nm) Schottky metal are done by lift-off techniques, respectively. Then, a 210 nm thick silicon nitride is deposited at 250^o C on the surface of samples that is etched through by using photolithographically defined resist as a mask. The next step is definition of posts of air-bridges. In this process the resist is hard baked after the photolithography as explained previously and then thinned down to 800-900 nm by RIE (Reactive Ion Etching). Final step is definition of air-bridges by photolithography and deposition of Ti/Au (10-15/1000 nm), by lift-off technique. In this last step, the spun resist will not dissolve the post resist because of the hard bake. If all the above steps are successfully completed, we will hopefully have properly working devices, which is a first step goal of this work. The schematic cross section of a typical photodiode is shown in Figure 3.3 and microphotographs are seen in Figures 3.4 and 3.4.

3.7 I-V Tests

The first check of the process is the I-V test of the finished diodes. If good Schottky characteristics are observed, those diodes can be considered for further characterizations. A good Schottky diode should have high reverse breakdown voltage, low saturation current, and low threshold voltage. In Figure 3.6 , an I-V curve of a diode (on NIST wafer, $100 \times 120\ \mu m^2$) is shown. Typical breakdown voltages were around 2-3 volts for large area (50×70 to $400 \times 400\ \mu m^2$) NIST diodes. For small area diodes (7×7 to $20 \times 30\ \mu m^2$), breakdown voltages were around 10-15 volts. The ISU diodes had breakdown voltages very similar to the NIST diodes. The reverse breakdown voltage is low due to relatively high carrier concentrations ($\sim 10^{17}\ cm^{-3}$) which causes an early avalanche.[3] Saturation currents measured for large area diodes were lower than around 1 nA, a few pA for best ones. Threshold voltages of all properly working diodes were below 0.7 volts. Ideality factors were calculated to be around 1.2-1.3, which point out the existence of a tunneling component along with the thermionic current. Built in potentials were around 0.65-0.7 volts, which were in the expected range.

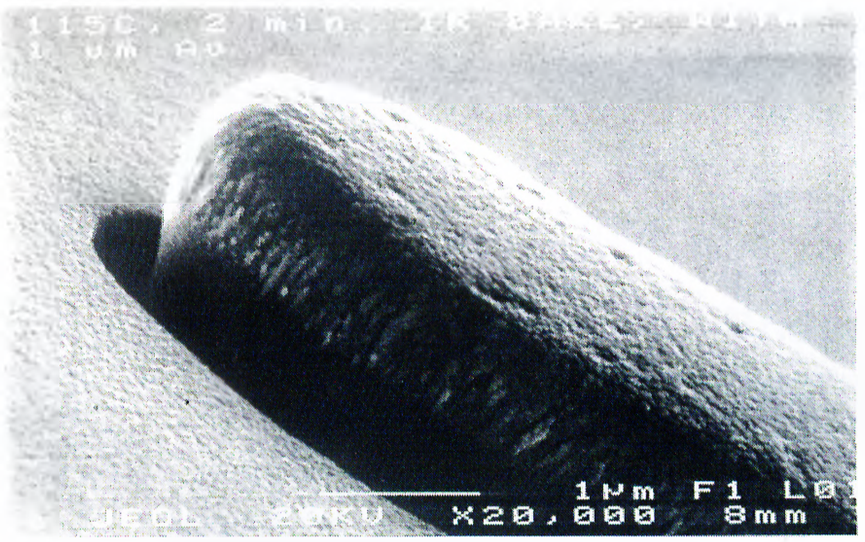

Figure 3.1: SEM photo showing Au deposited on image-reversed resist line. The surface of the sample is totally coated by (snowy looking) gold. The undercut of the resist and gold deposited on top can be seen clearly.

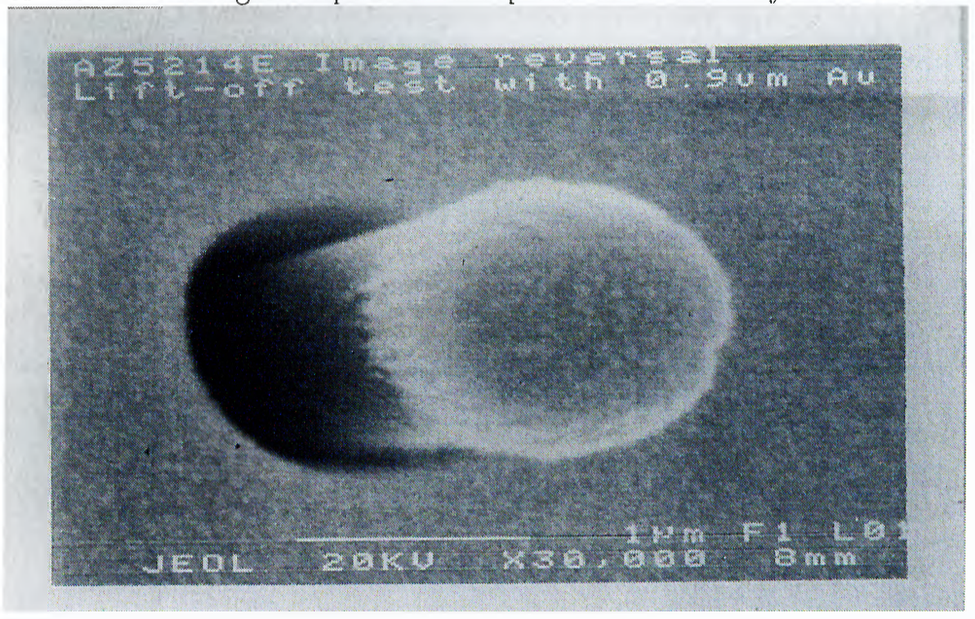

Figure 3.2: SEM photo showing Au deposited on image-reversed dot-shaped resist.
The surface of the sample is totally coated by (snowy looking) gold. The mushroom shaped structure is gold on top of resist. The resist is like a upside-down cone with approximate diameter of 1μm.

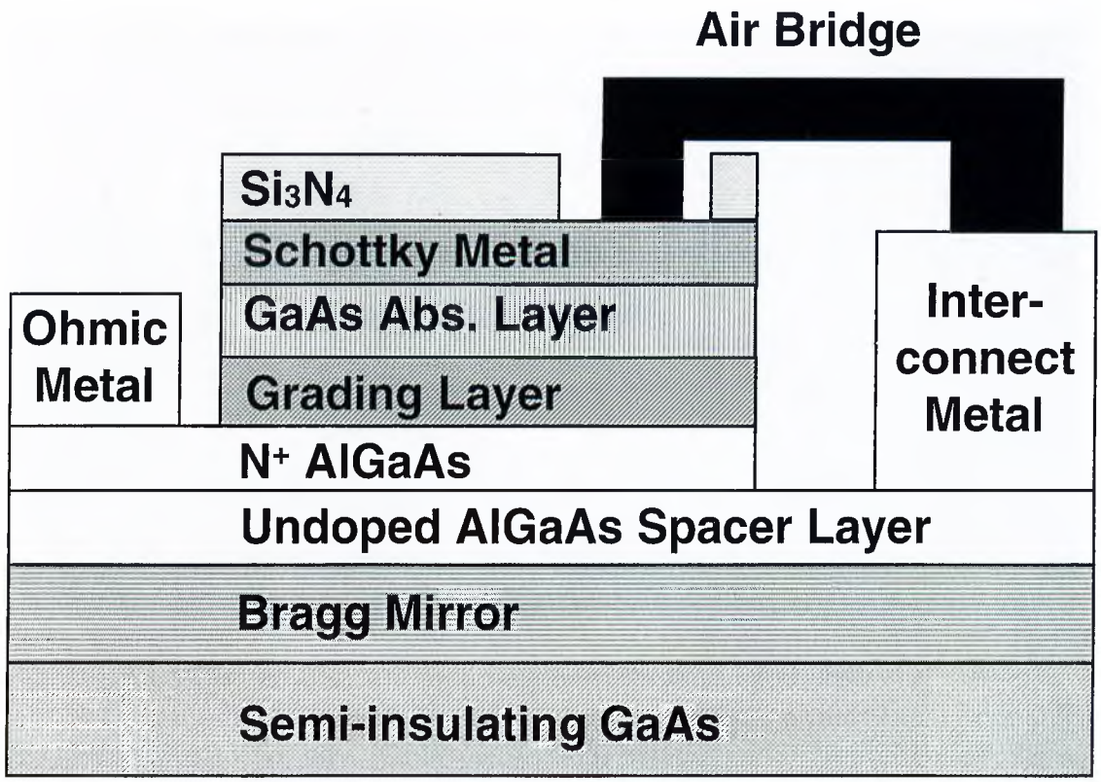

Figure 3.3: Schematic cross section of a fabricated RCE photodiode

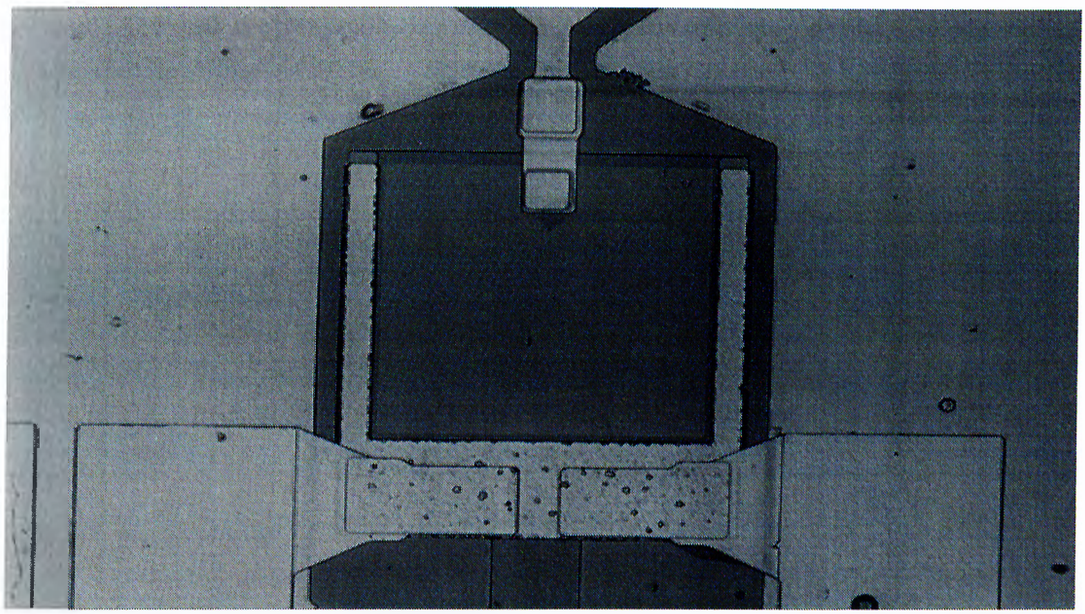

Figure 3.4: Microphotograph of a fabricated device
At the top air bridges connections between the top plates of bias capacitors and the ohmic contact are seen. CPW comes from bottom and its center conductor is connected to the Schottky contact by an airbridge. There are two bias resistors in between central and ground conductors of the CPW.

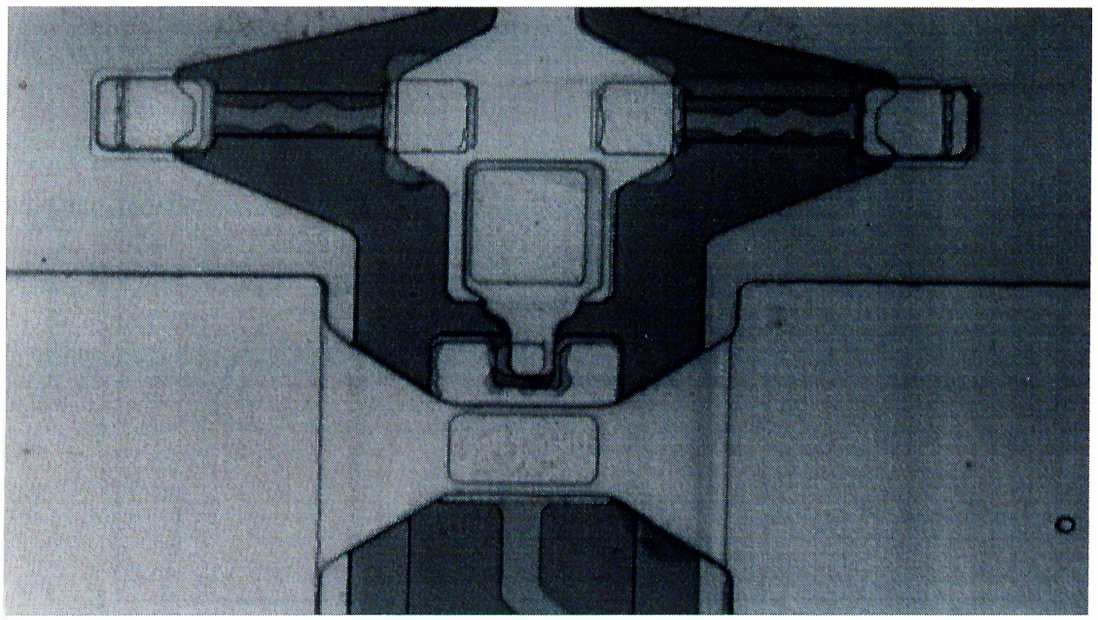

Figure 3.5: A microphotograph of another type of a fabricated device Four airbridges and large top plates of bias capacitors are seen.

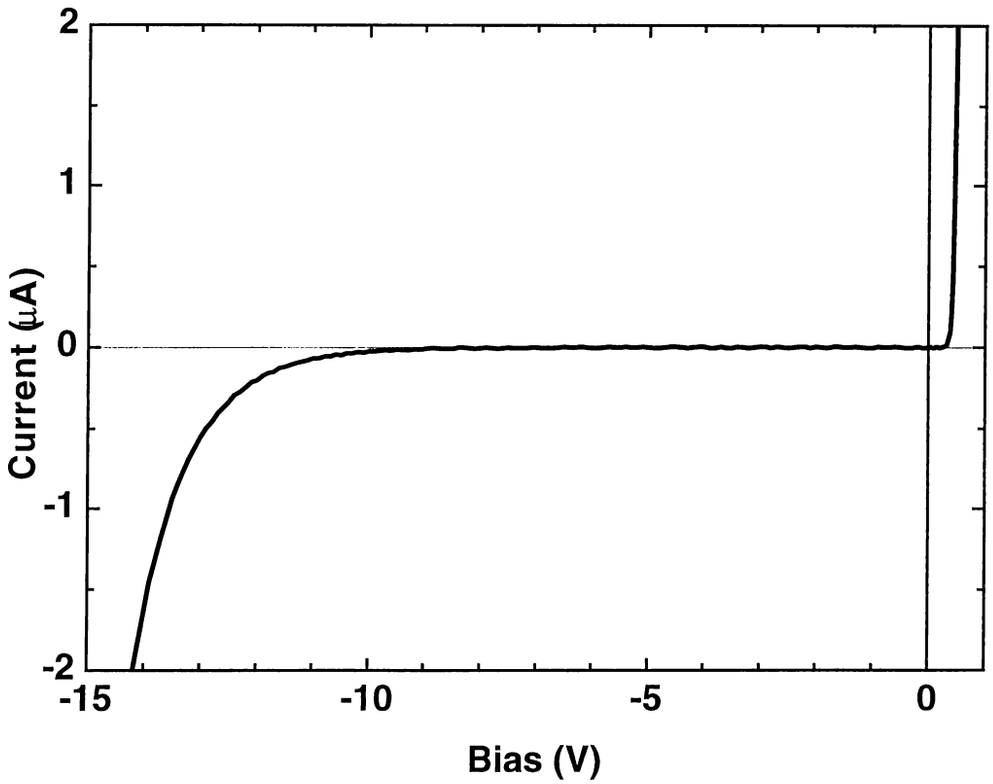

Figure 3.6: A typical I-V curve

Chapter 4

Measurements

Basic characteristics of a photodiode were discussed in Chapter 2. In this chapter, we present measurements performed on the fabricated diodes. Except for the high speed measurements, all measurements were performed in our laboratory. Although measurements can be explained in short paragraphs, in fact they usually took more time than the fabrication. Optimization of the setup, the search for best measurement parameters (such as lock-in amplifier integration time, bias, *etc.*) for individual diodes, and the optimized form of the photoresponses of photodiodes by multistage recess etchings took considerable amount of time. The reflection spectrum of samples were determined by using a spectrometer embedded on a personal computer card. HP 4142B model modular DC source-monitor system was used for biasing the diodes probed on an Alessi probe station. Spectral quantum efficiency measurements were carried out by using a Digikrom DK840 model monochromator and a SR850 model digital lock-in amplifier. High frequency measurements were carried out at Photonics Research Laboratory of Boston University.

4.1 Reflection Spectra of Bare Samples

Prior to fabrication processes reflection properties of each sample were determined by a reflection spectrometer. These measurements not only enabled us to

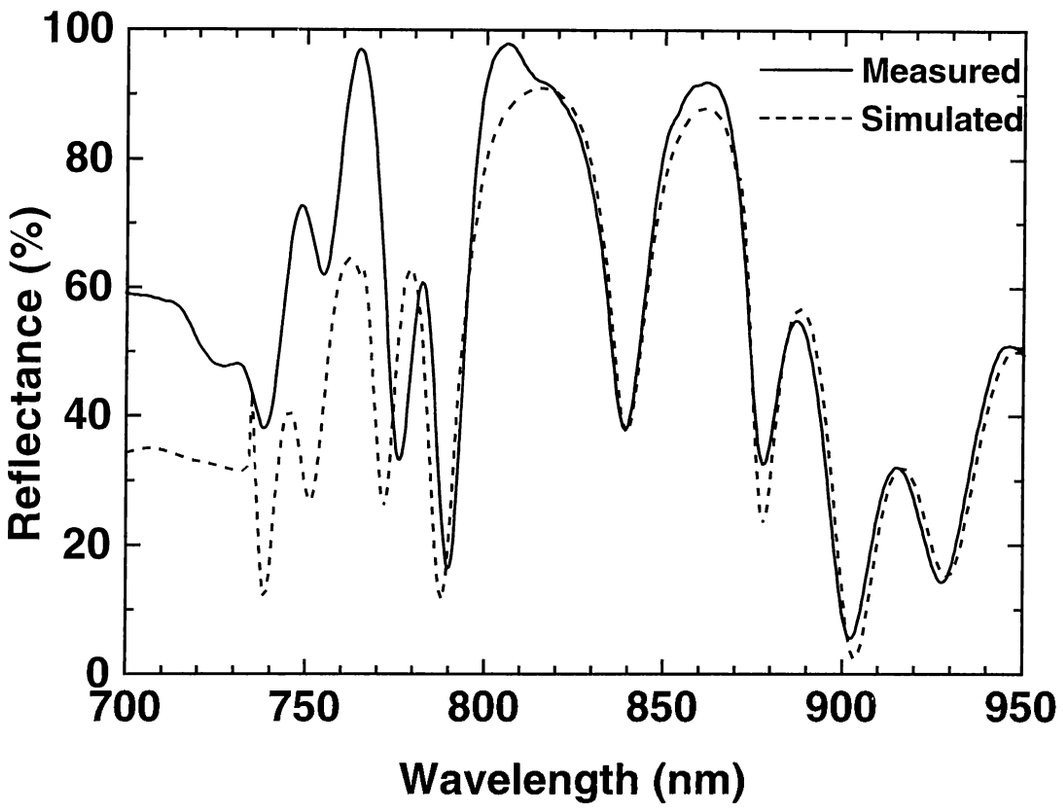

Figure 4.1: Measured and simulated reflection spectra of the NIST sample.

determine the resonance wavelength, but to some extend, enabled us to vary the resonance spectrum, as well. These spectra were also used as a basis in our simulations from which we, for example, extracted actual layer thicknesses.

4.1.1 NIST samples

Reflection spectra of NIST samples (see Table 3.1 for the structure) were consistent for all parts of the wafer (within a few percent). Measurement and fitted simulation spectra are given in Figure 4.1. The simulations were done by using scattering matrix[39,34] (S-matrix) and transmission matrix formalism.[40] In the measured spectrum, it can be seen that the resonance occurred at 840 nm. Around the wavelength of interest, the theory and experiment fits very well.

4.1.2 ISU samples

The reflection spectra of ISU samples were not so consistent for different parts of the wafer, as compared to NIST wafer. However, ISU had the advantage of wavelength tuning by wet chemical etching of 330 nm thick cap layer (see Table 3.2). If the reflection spectrum of an ISU sample was observed not to satisfy our requirements, we had the option to etch its cap layer until we obtained the desired resonance (at around 850 nm). By using an ammonium hydroxide: hydrogen peroxide: DI water (7: 1.2: 400 volume ratio) etchant, we tuned the resonance wavelength within a few nm of desired wavelength. The bare ISU samples were tuned to 840-850 nm, since it was observed that the deposition of a 10 nm Au resulted in approximately 8-9 nm blue-shift of the resonance wavelength (see section 4.2).

In Figure 4.2, reflection spectra of an ISU sample, measured along with corresponding fitted simulation data, are presented. The discontinuities at about 870 nm in this and forthcoming simulations are due to the sharp discontinuity, of the data used for GaAs refractive index, at the bandgap edge. The positions of the measured minima and maxima are consistent with simulations. In Figure 4.3, measured reflectivities of an ISU sample, which was used for fabrication of actual devices, are presented. This sample, which at first was not suitable for 840 nm operation (dashed line), was tuned, by removing approximately 40 nm of cap layer in several etch steps, for operation wavelength (solid line) as mentioned above.

We also tuned another set of ISU samples with different absorption thicknesses. We named these samples as S1, S2, and S3 for brevity. These samples were prepared to study the affect of absorption layer thickness on RCE photodiode performance. Each of these samples were carefully tuned for 850 nm resonance. Tuning of S1 was the same as explained in the preceding paragraph. However, for S2 sample after observing first resonance reflection minima, we continued to etch till we tuned the sample to second resonance (again at 850 nm). Similarly, S3 is tuned to third resonance, at 850 nm wavelength. Absorption layer thicknesses of S1, S2, and S3 were determined (from theoretical fits to corresponding reflection

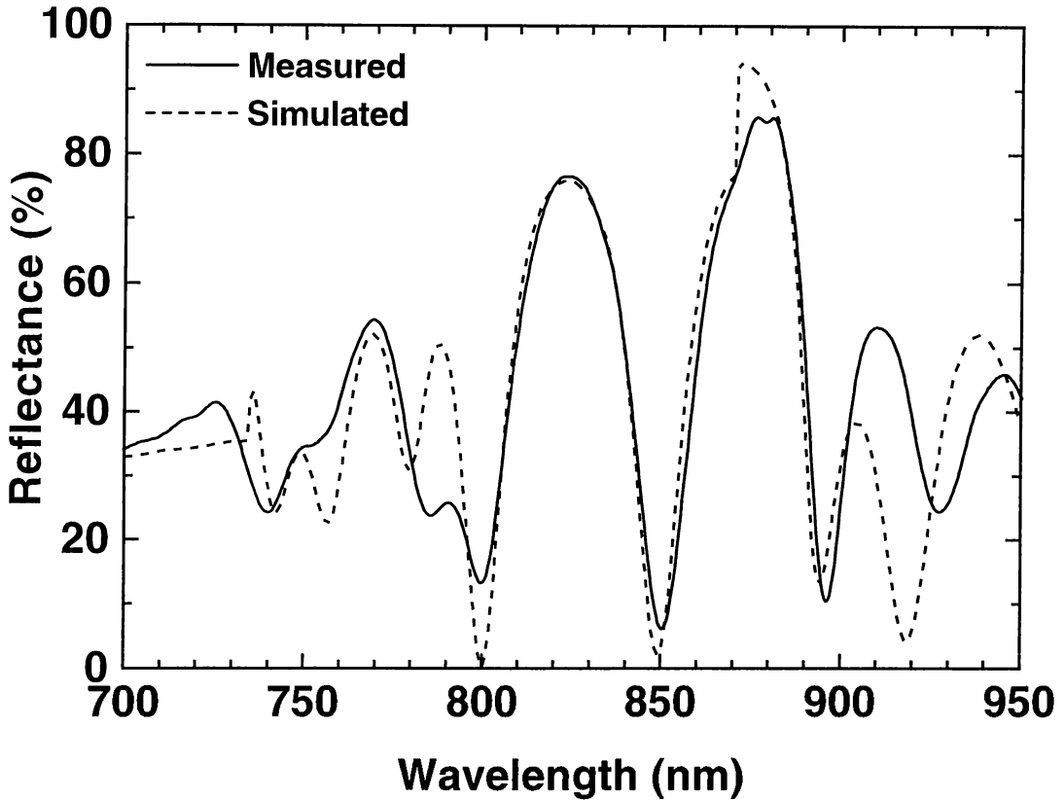

Figure 4.2: Measured and simulated reflection spectra of the ISU sample.

spectra) as 290, 175, and 60 nm respectively. These samples were also processed as defined in Chapter 3.

4.2 Effects of Schottky Contact and Silicon Nitride

We also carried out another set of experiments to understand the effects of, thin Schottky contact and nitride overlay, on the reflection spectrum. These experiments were carried out on ISU samples only, since we had only a small portion of the NIST wafer. We cleaved four pieces of the ISU wafer, and deposited approximately 7, 12, 17, 21 nm gold on each, and then 210 nm of nitride. Then this nitride layer is thinned in approximately 20 nm steps, until it

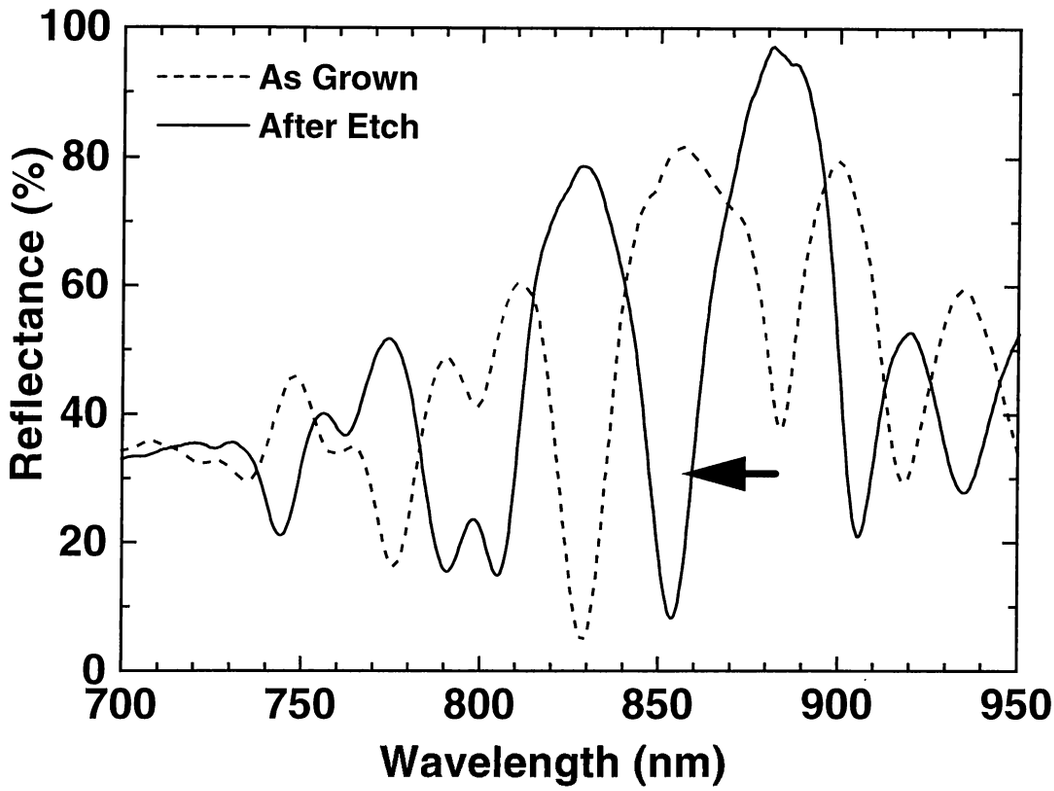

Figure 4.3: A set of reflection spectra of the ISU sample.
The dashed line corresponds to the spectrum of the as-grown sample, whereas the solid line corresponds to the spectrum after wavelength tuning by wet chemical etching of the cap layer by approximately 40 nm.

is totally removed in twelve steps. In Figure 4.4, reflection spectra of one of these samples are presented. The "Bare" spectrum belongs to an as-grown sample, with 6% reflection minimum at 850 nm. The "+7 nm" spectrum belongs to the same sample after a deposition of approximately 7 nm of gold, which shows an absorption dip of 11% at 845 nm. Then an "210 nm SiN" (silicon nitride) is grown which moved the resonance to 842 nm (12.8%). After the fourth etch, which recessed the nitride layer to approximately 1300 nm thickness, minimum reflectivity of 2.4 % at 843.5 nm was observed.

Another set of simulated reflection spectra is presented in Figure 4.5. Theoretical reflectance minimum is 1.5% at 827 nm, which is blue shifted to

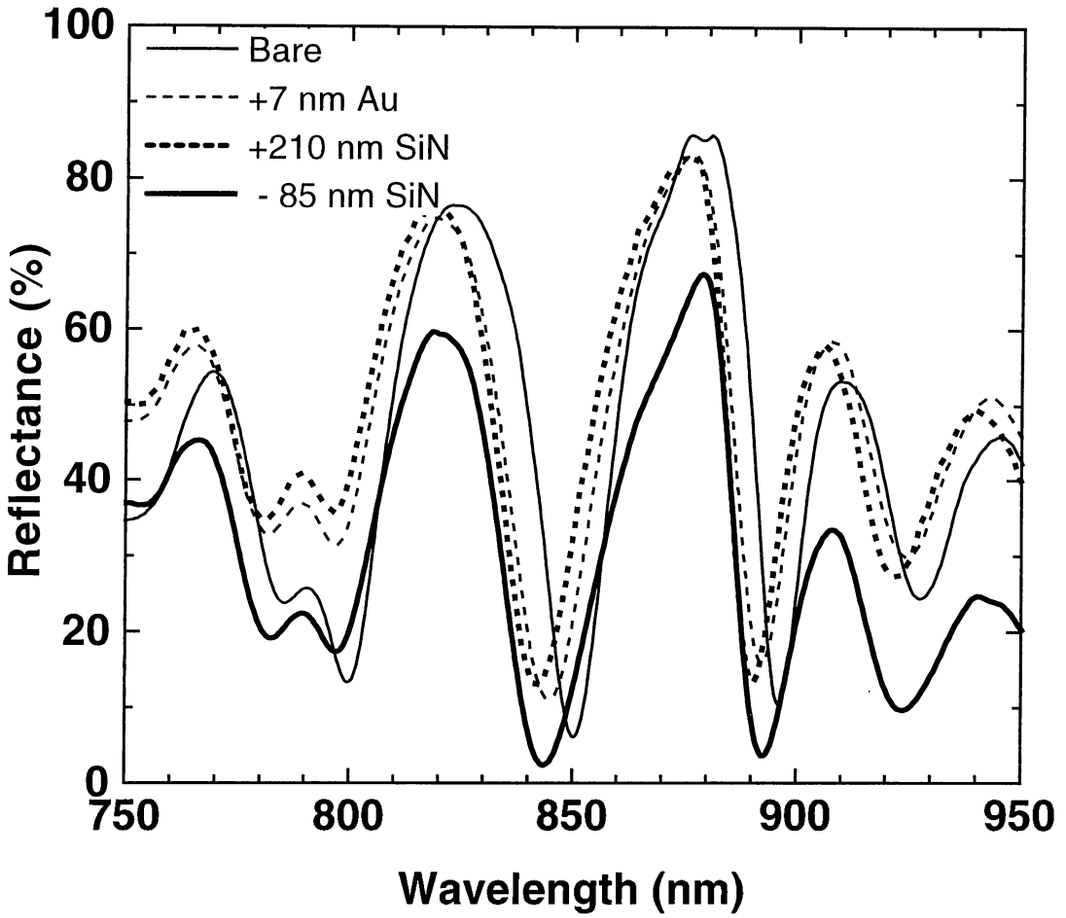

Figure 4.4: A set of reflection spectra of the ISU sample with overlaying thin films.
"Bare" corresponds to bare sample prior to fabrication. "+7 nm Au" corresponds to the effect of 7 nm Au deposition. "+210 nm SiN" corresponds to an additional 210 nm nitride layer. "-85 nm" corresponds to the fourth etch step, by which nitride layer is recessed down by 85 ∓ 5 nm.

4.5% at 819 nm after addition of 10 nm thick gold layer. Further addition of a 130 nm nitride layer yields 3.4% minimum at 816 nm. By considering these and other measurement and simulation data, we can conclude that reflection minima (absorption maxima) blue-shift (non-linearly) depends on deposited gold thickness. This shift is approximately 8-9 nm for 10 nm gold deposition, and saturates at approximately 10 nm for thicker gold depositions.

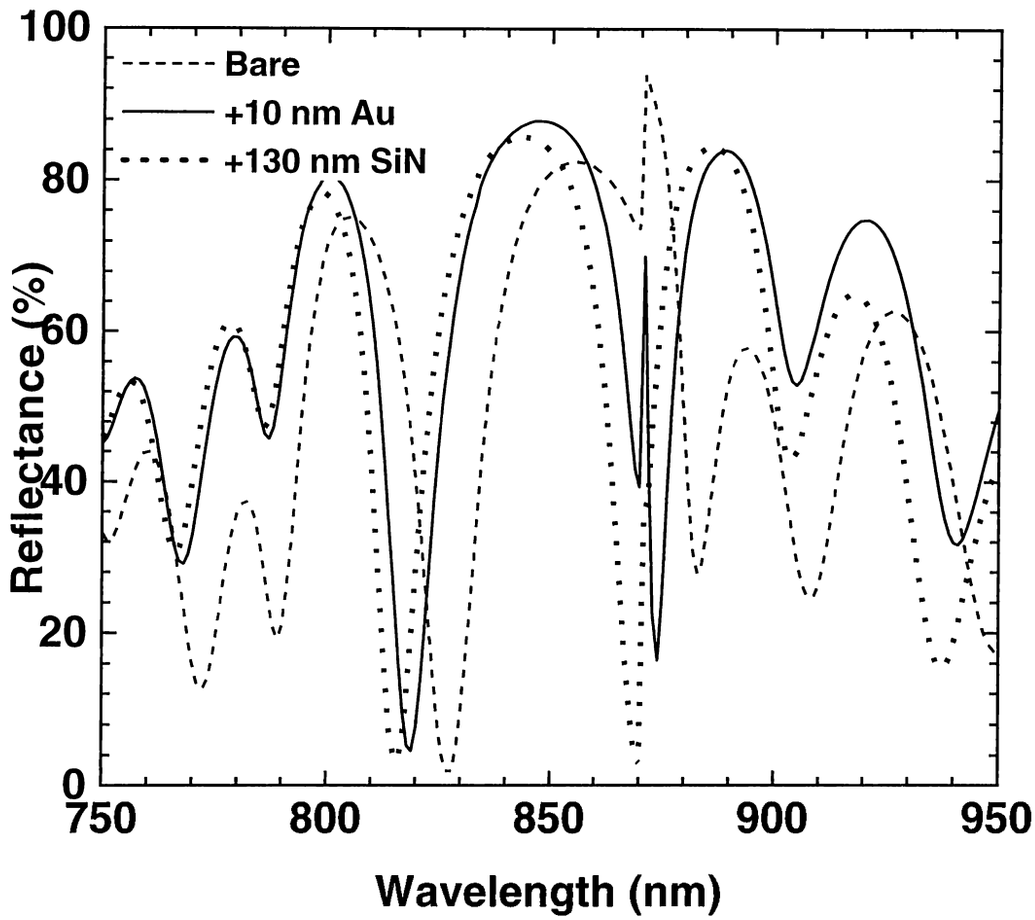

Figure 4.5: Simulated reflection spectra of the ISU sample with various films. "Bare" corresponds to the bare ISU sample. "+10 nm Au" corresponds to ISU sample coated with 10 nm of Au. "+130 nm SiN" corresponds to an additional 210 nm nitride layer.

Magnitude variation of reflection shows a complex and hard to predict dependence on gold thickness. Reason for inconsistency is most probably due to the unpredictable scattering losses at the rough surface of Au film.

Silicon nitride layer mainly alters the magnitude of reflectance, the dip position shift is less than 0.5% for various nitride thicknesses (less than 210 nm). Thus, it is possible to vary the thickness of this dielectric layer as a tool for photoresponse optimization.

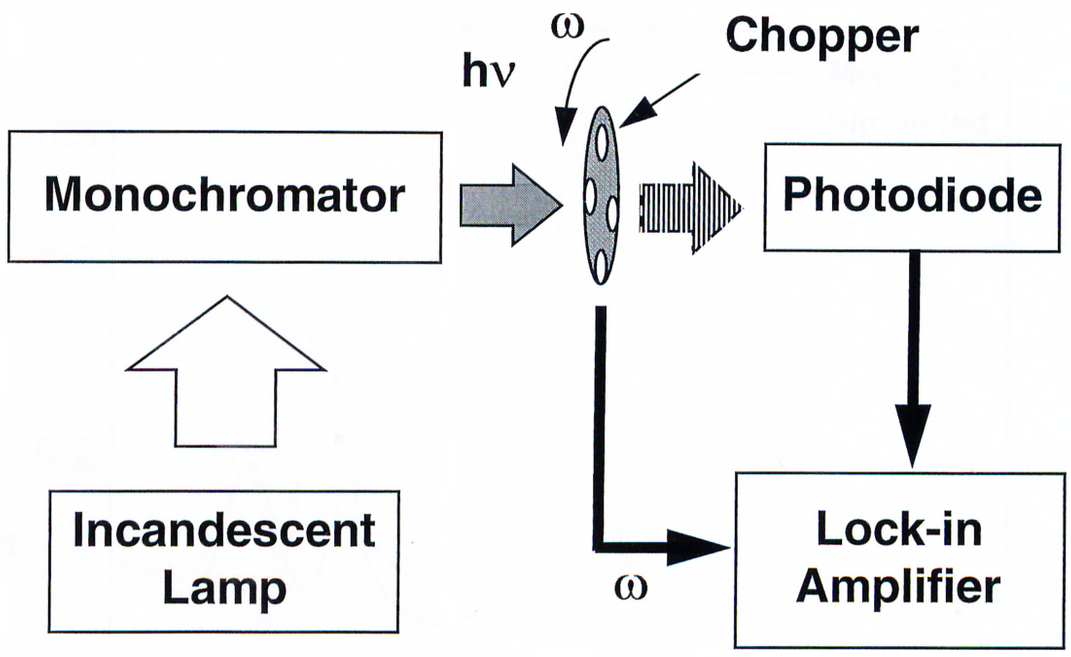

Figure 4.6: A schematic diagram of quantum efficiency measurement setup.

4.3 Photoresponse Measurements

Definition of quantum efficiency was given in section 2.1. Thus our aim is to determine the optical wavelength dependence of the photo-current versus the incident optical power on the photodiode. The quantum efficiency setup is explained briefly by a schematic diagram in Figure 4.6. The incandescent light source is a tungsten-halogen lamp. The monochromatic light output of the monochromator was delivered to the photodiode by a lightwave fiber probe coupled to a single mode optical fiber. This fiber probe, like electrical bias and measurement contacts, was attached to a probe station on which all the measurements were carried out. A mechanical (wheel) chopper was introduced in the optical path by using microscope objectives as optical fiber couplers. Chopping frequency was kept around ~ 330 Hz. The core diameter of the lightwave fiber probe was 62.5 μm, which limited the quantum efficiency measurements to the photodiodes with areas 400×400, 250×250,150×150, and $100 \times 120 \mu m^2$.

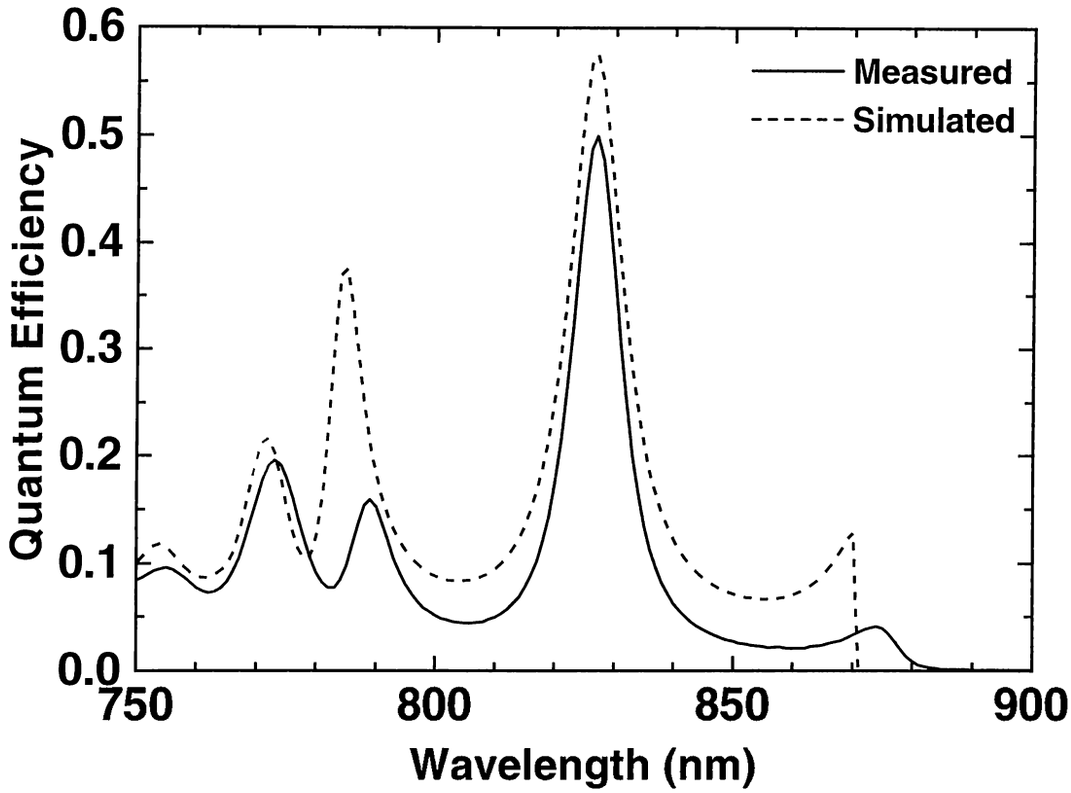

Figure 4.7: Measured and simulated photoresponses of the NIST sample.

Another important issue of the measurements was the final optimization of the photoresponses by etching the top silicon nitride layer as mentioned in section 4.2. The grown nitride thickness was chosen to be 210 nm, which corresponds to a $\lambda/2$ optical thickness (at 840 nm, $n_{nitride}$=2). Recess etching was done by a dilute hydrofluoric acid etchant, in 20-25 nm steps, while determining the photoresponse after each etch, until peak efficiency was reached (i.e., efficiency started to decrease). During these etchings, observed peak efficiency wavelength shifts were not significant (less than 1 nm) as expected.

4.3.1 NIST sample

In Figure 4.7 measured and simulated photoresponse spectra of the NIST sample are presented. For the actual sample, the silicon nitride layer was etched down

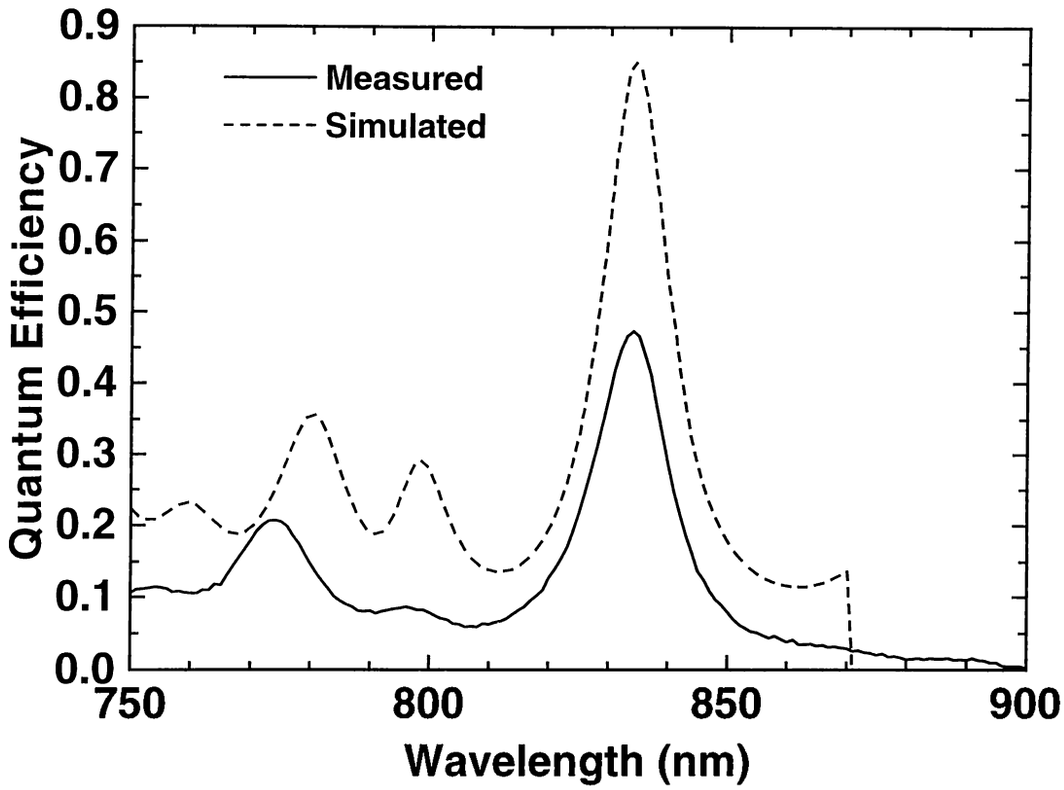

Figure 4.8: Measured and simulated photoresponses of the ISU sample

by approximately 60 nm, thus 150 nm nitride thickness was assumed in the simulations. Peak positions are consistent with the simulation. The measured 50% and simulated 58% peak efficiencies are both observed at 827 nm.

4.3.2 ISU sample

For the ISU sample (see Figure 4.8), since we have changed the cap layer thickness prior to the process, simulation is fitted to the measurement by corresponding modification of structure. The nitride thickness was chosen to be same as 130 nm which optimized the actual photoresponse. The measured peak quantum efficiency was 47% at 834 nm, not comparable with that of simulation, 85% at 834 nm. When compared to single pass structures, approximate enhancement

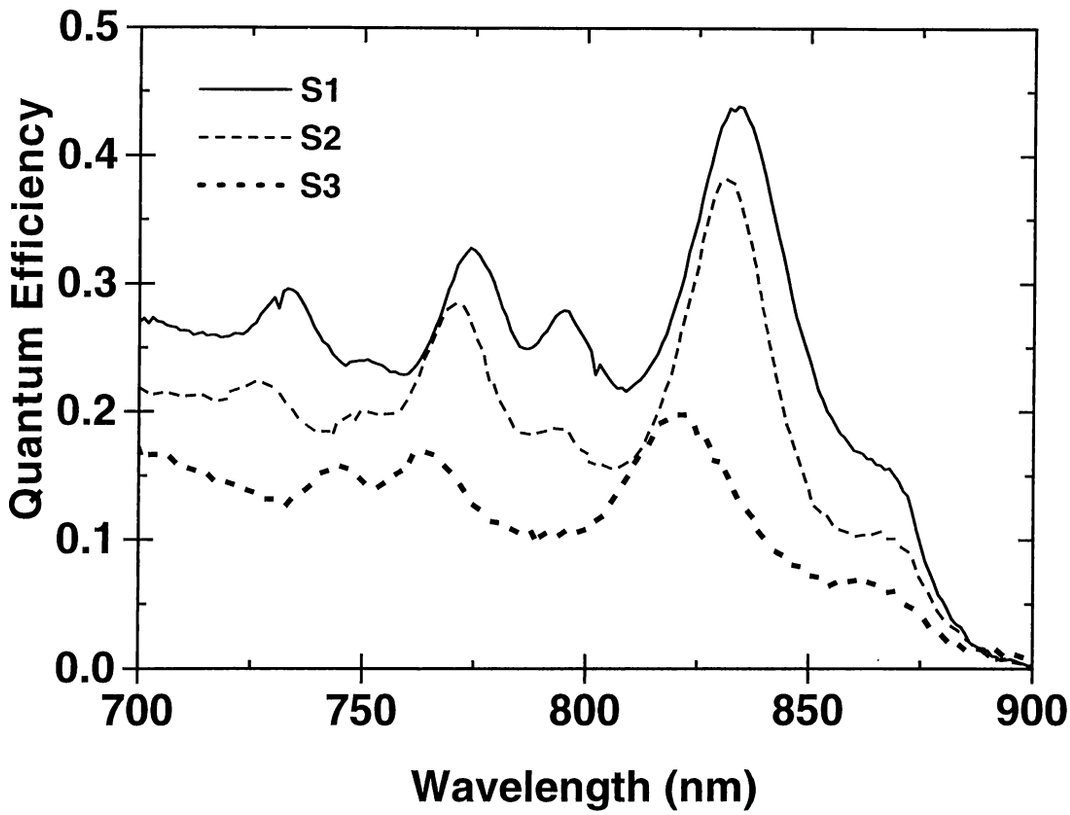

Figure 4.9: Measured photoresponses of the S1, S2, and S3 samples Peak efficiencies are 44% at 835 nm, 37% at 830 nm, and 20% at 825 nm for S1, S2, and S3, respectively.

factors are 16 and 8 for the NIST and ISU samples, respectively. The higher off-resonance photoresponse (hence lower enhancement) of the ISU sample is a result of thicker absorption layer as compared to the NIST sample. The full-width at half maximum (FWHM) is 10 nm for the NIST and 9.5 nm for the ISU sample.

Photoresponses of samples S1, S2, and S3 are shown in Figure 4.9. Peak quantum efficiencies for samples S1, S2, and S3 were 44%, 37%, and 20%, respectively.

4.3.3 Surface roughness problem

Observed photoresponses of the photodiodes were poorer than expected. Although we revised the simulations and did the fabrications several times, the difference between theory and experiment (though varying) was larger than we expected. After various attempts to explain the difference, we decided to check the Au surfaces. We evaporated various thicknesses of Au on GaAs samples, and observed the Au surface by an atomic force microscope (AFM) at Boston University.

In Figures 4.10 and 4.11 three dimensional AFM surface scan of 15 and 10 nm thick evaporated Au layers are seen, respectively. The surface roughness of the 15 nm sample was measured as 1.2 nm (corresponds to a few Au atoms), which was fairly good. However, surface roughness of the 10 nm sample was very large, 7.4 nm. Similar measurements were performed on other samples also. Surface roughness measurements have shown that, roughness did not have any clear dependence on thickness. According to AFM measurements we decided that evaporated Au had rough surface, and this roughness depends on evaporation parameters that seems to be varying during each deposition. Possible causes of roughness may be poor Au source quality, uncontrolled process parameters such as evaporation boat temperature, partial vacuum of Au during evaporatin, etc. Considering the highly random surface roughness of Au layers, we conclude that large portions of the differences between theoretical and experimental diode responses are due to scattering losses at Au surface.

4.3.4 Bias dependence

All the data discussed above were for devices measured under zero bias. The bias dependence of the NIST sample is presented in Figure 4.12. The 46% efficiency at 827 nm, increases to 47% for -1.5 V and 48% for -2.2 V biases, respectively, both at 828 nm. Further increase in reverse bias results in a sudden increase in efficiencies of both samples. For example, at -2.5 V, 56% peak quantum efficiency was observed in the NIST sample. Quantum efficiency beyond 100% is reached with

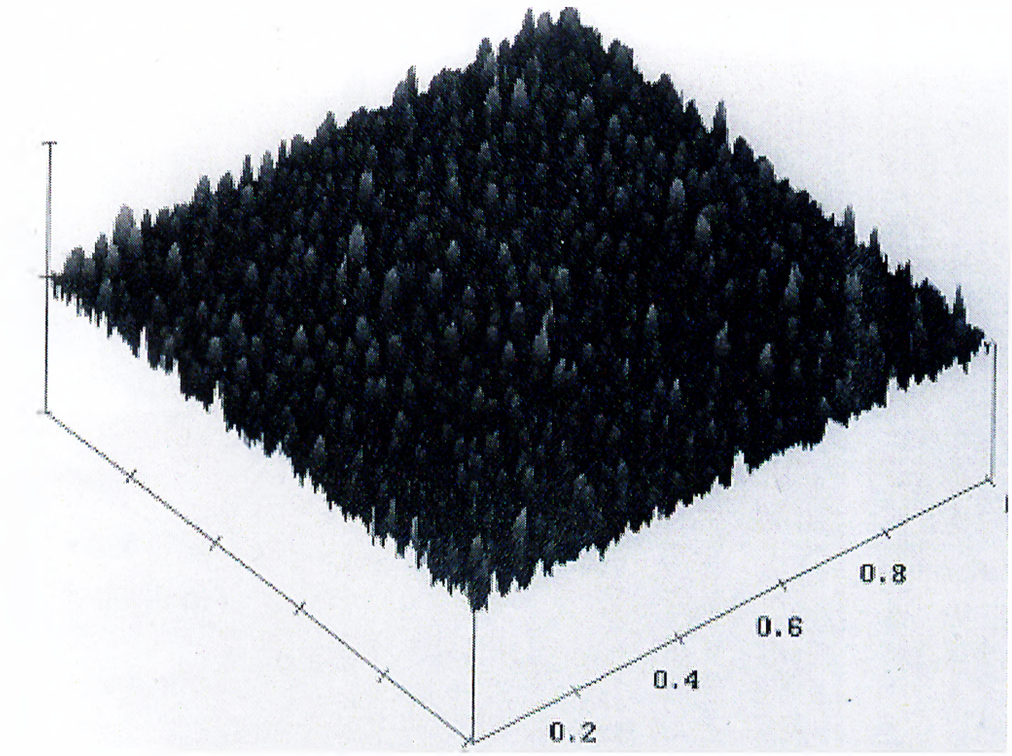

Figure 4.10: AFM image of 15 nm Au film evaporated on GaAs.
X and Y scale divisions are 0.2 μm, Z scale division is 25 nm. Au island formation is low.

-2.7 V bias. This feature is attained to an early breakdown gain, like an avalanche photodiode (APD). APDs attain very high quantum efficiencies due to avalanche multiplication of photogenerated carriers. Similar results were also observed for the ISU sample, with about -1.7 V gain threshold voltage (not presented here). The minor dependence of photoresponse on reverse bias can be explained as the result of weak dependence of depletion layer width on bias potential V (see Equation 2.3) due to the relatively high donor concentrations of the structures.

4.4 High Speed Measurements

High speed measurements were done at the Photonic Research Laboratory of Boston University. A schematic diagram of the measurement setup is shown in

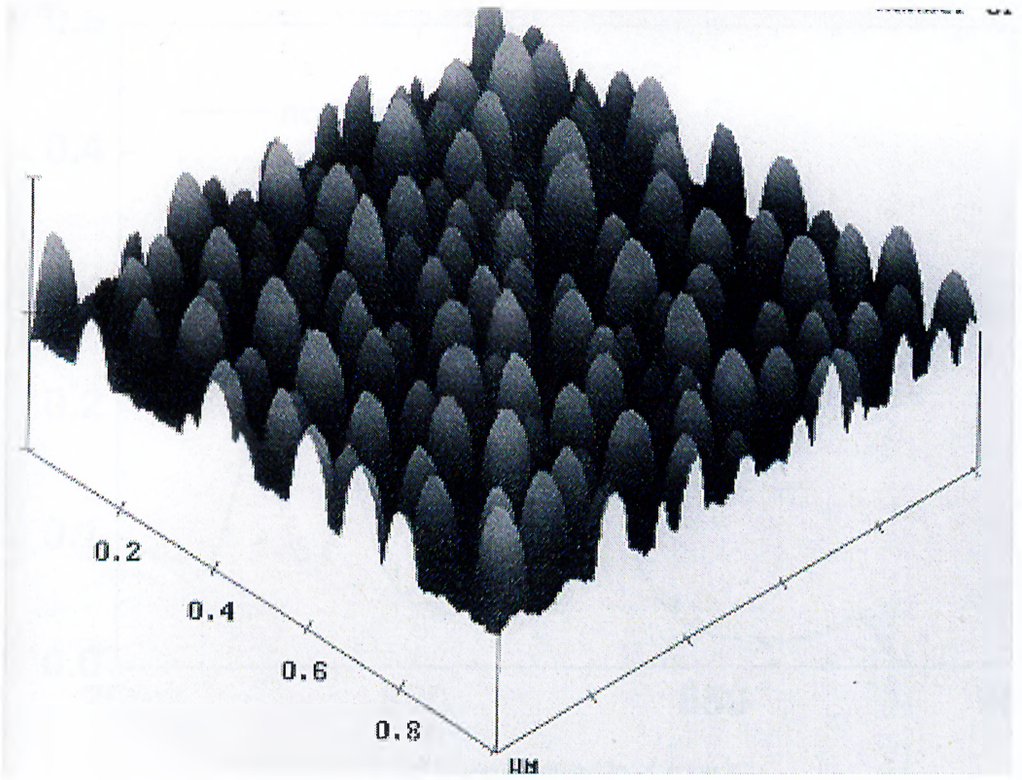

Figure 4.11: AFM image of 10 nm Au film evaporated on GaAs. X and Y scale divisions are 0.2 μm, Z scale division is 50 nm. Au island formation is very high.

Figure 4.13. The mode locked laser is a Ti: Sapphire laser (Coherent Model Mira 900) which delivered 1 ps pulses for our measurements. The sampling oscilloscope is a 50 GHz HP54120B, connected to the photodiode via microwave probes on a probe station.

4.4.1 NIST pulse response

In Figure 4.14, the temporal response of a small area photodiode (8×14 μm) on the NIST sample is presented. The measured photodiode output has a 13 ps FWHM, and a fall time of 7 ps. The Fourier transform of the response, as plotted in Figure 4.15, shows a 3-dB bandwidth of 41 GHz. On the same figure, theoretical fit to the experiment is also plotted (dashed line) as explained in

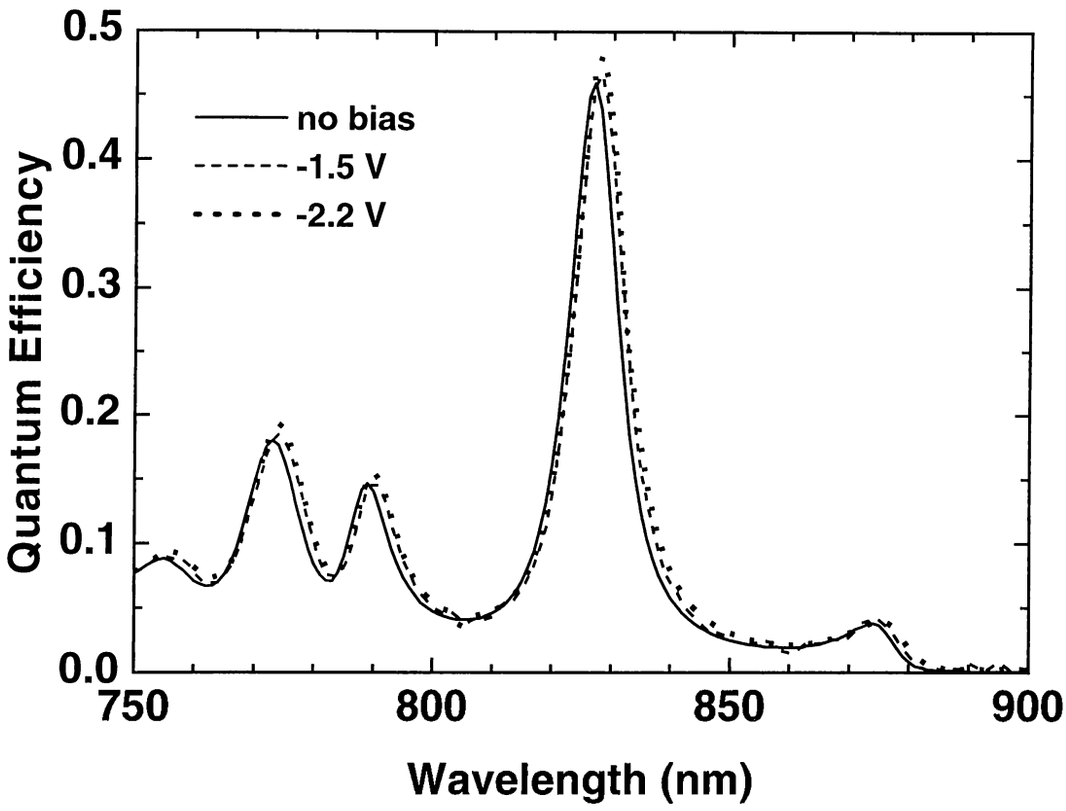

Figure 4.12: Bias dependence of the photoresponse of the NIST sample.

section 2.5. The 50 GHz scope response was deconvolved and also plotted (dotted line) in the same figure. Deconvolved response shows that actual bandwidth of the NIST sample is 78 GHz.[31,41,42]

4.4.2 ISU pulse response

In Figure 4.16, the temporal response of a small area (8×14 μm) photodiode on S2 sample is presented. The measured photodiode output has a 12 ps FWHM. The Fourier transform of the response, as plotted in Figure 4.17, shows a 3-dB bandwidth of 40 GHz. On the same figure, theoretical fit to the experiment is also plotted (dashed line) as explained in section 2.5. The 50 GHz scope response was deconvolved and plotted (dotted line) also. Deconvolved response shows that actual bandwidth of the S2 sample is 71 GHz.[31,41,42]

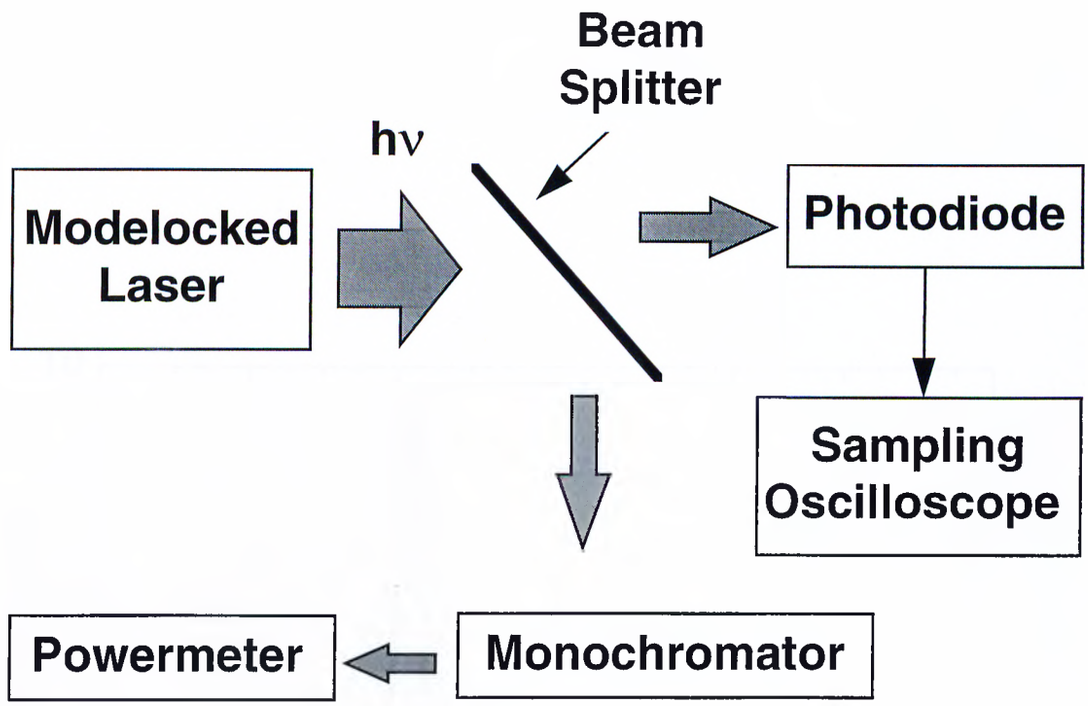

Figure 4.13: A schematic diagram af the high speed measurement setup.

Same deconvolution analyses for the S1 and S3 samples show that, corresponding bandwidths are 51 GHz and 110 GHz, respectively. Bode plots for simulated frequency responses of samples S1, S2, and S3 are shown in Figure 4.18.

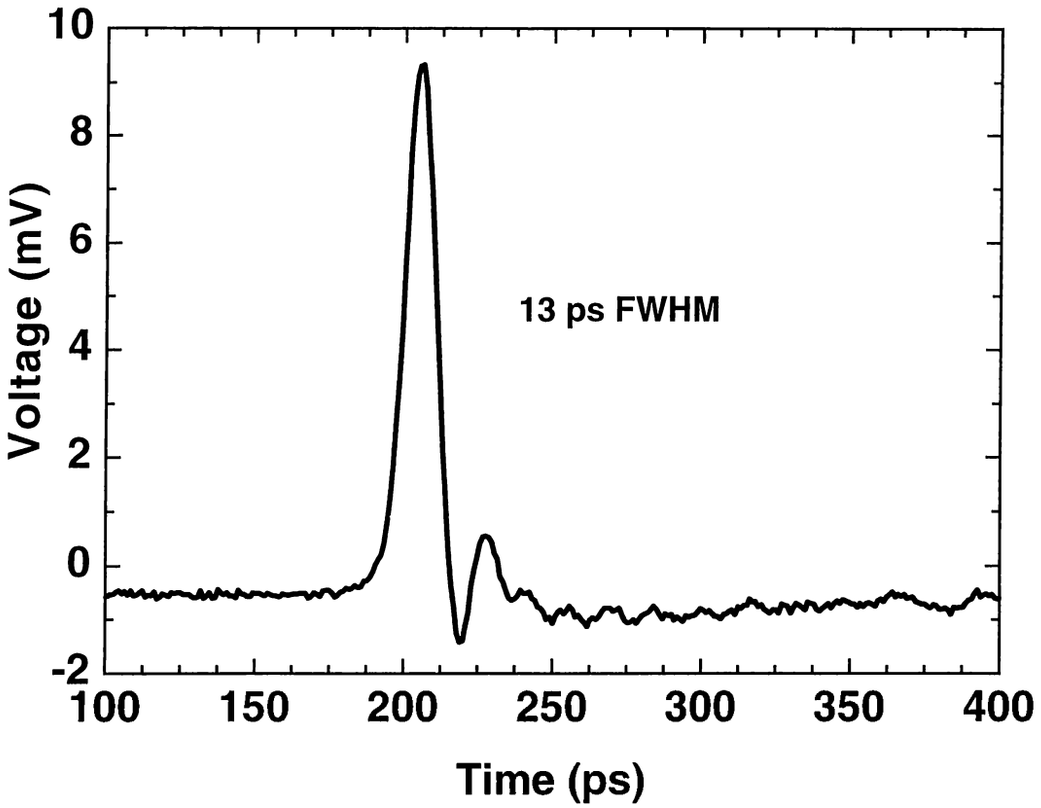

Figure 4.14: Pulse response of the NIST sample.

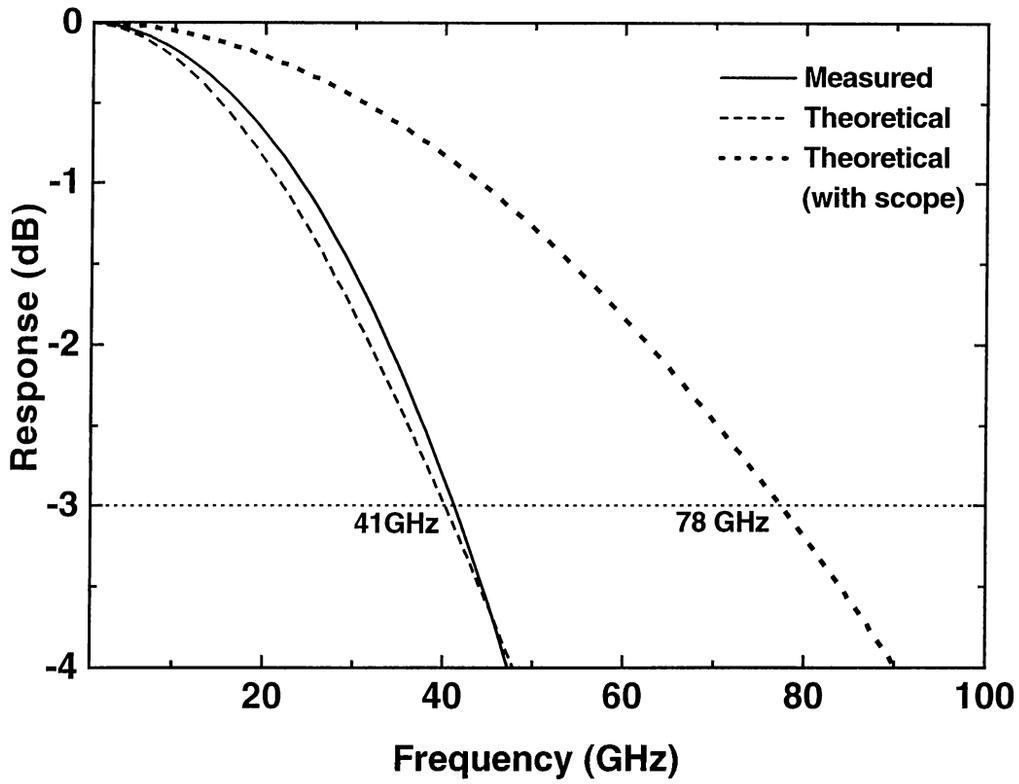

Figure 4.15: Experimental and theoretical Bode plots for the NIST sample. Measured (solid line) and corresponding fit (dashed line) with scope response included show bandwidth of 41 GHz. When the 50 GHz scope response is deconvolved, bandwidth is calculated as 78 GHz.

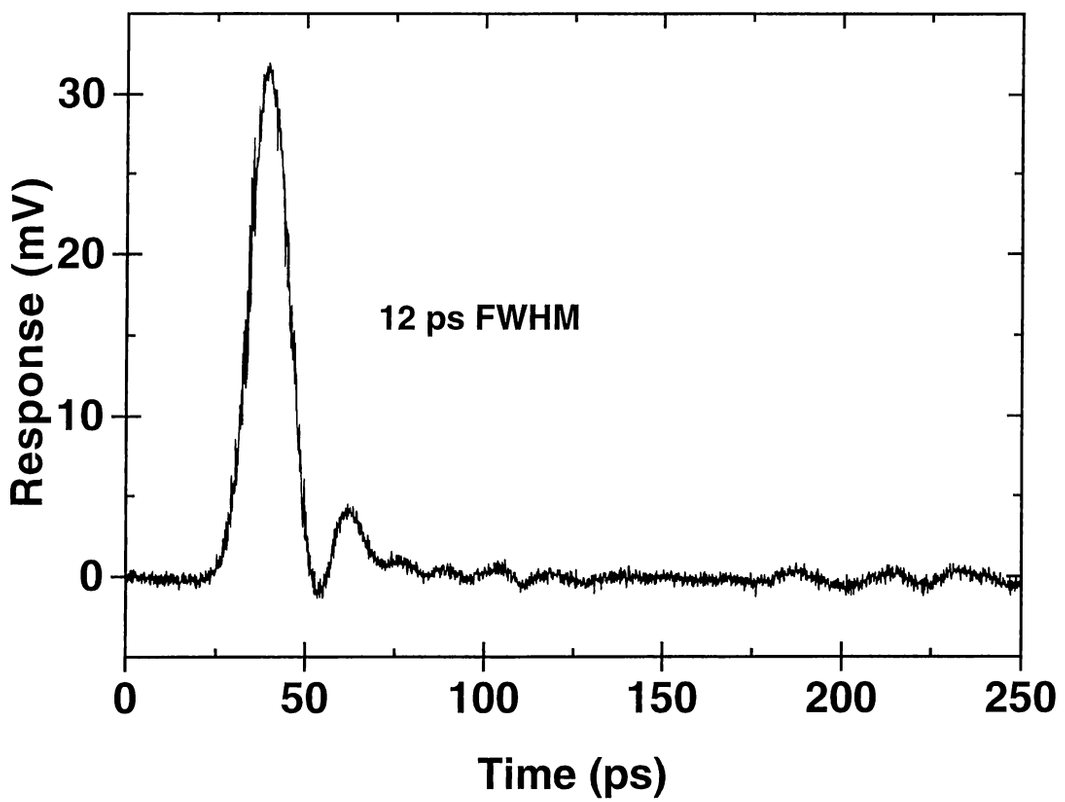

Figure 4.16: Pulse response of the ISU sample.

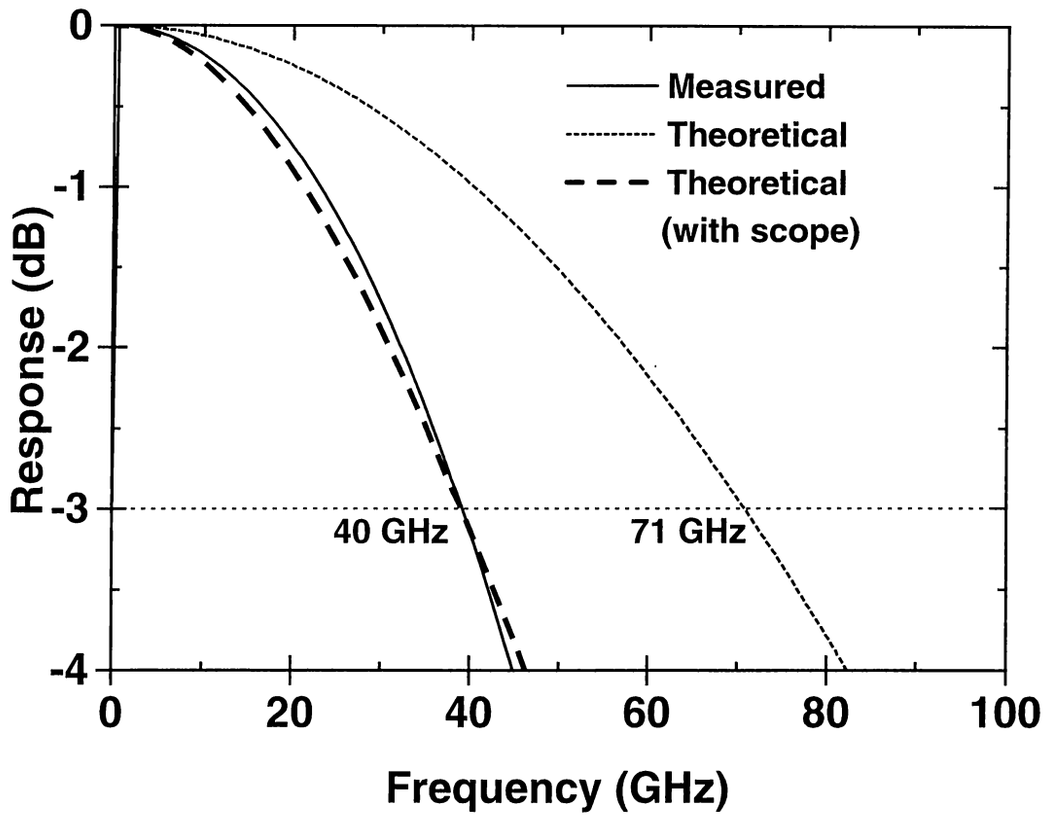

Figure 4.17: Experimental and theoretical Bode plots for the S2 sample. Measured (solid line) and corresponding fit (dashed line) with scope response included show bandwidth of 40 GHz. When the 50 GHz scope response is deconvolved, bandwidth is calculated as 71 GHz.

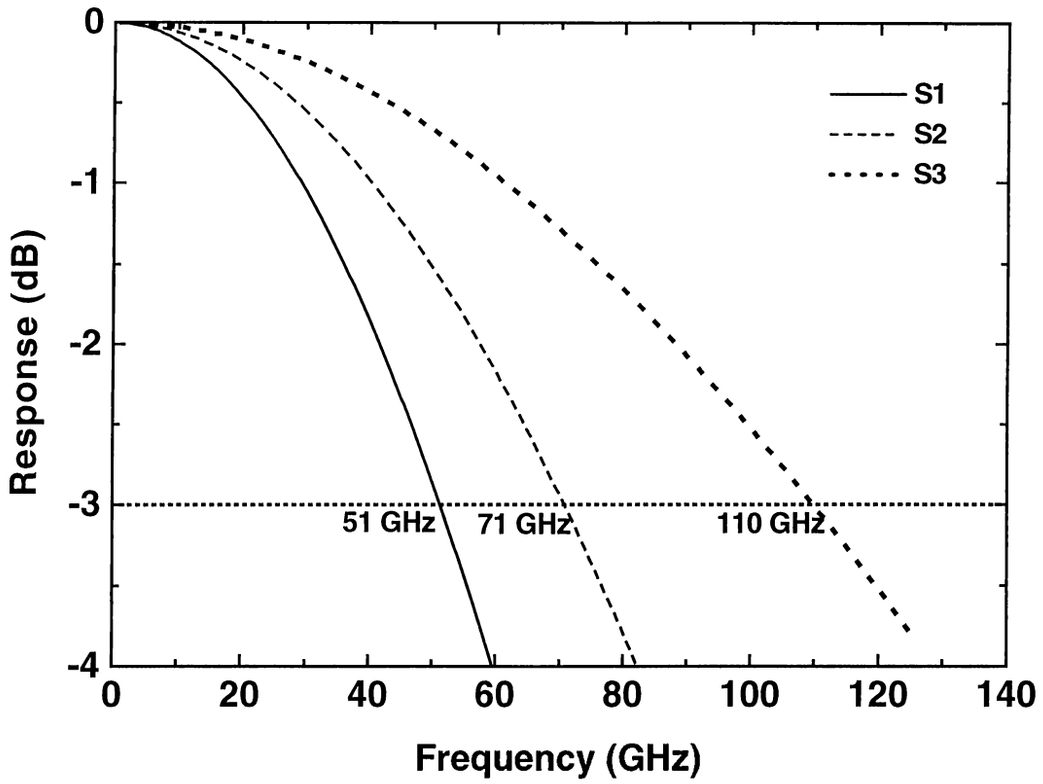

Figure 4.18: Theoretical Bode plots for the S1, S2, and S3 samples. S1 (solid line) has a theoretical bandwidth of 51 GHz. Similarly S2, and S3 have theoretical bandwidths of 71 GHz and 110 GHz, respectively.

Chapter 5

Discussions and Future Directions

Up to this point, we have given background information on RCE Schottky photodiodes, explained fabrication processes, and presented our experimental results.

The two photodiode structures we have fabricated consisted of GaAs/AlGaAs heterostructures, designed for operating at 800-850 nm wavelength. The NIST structure had a 120 nm thick GaAs absorption layer, which was 110 nm beneath the surface of wafer. On the other hand, the ISU structure had a 330 nm thick GaAs absorption region just on the surface of the wafer.

When compared to each other, within the perspective of our objectives, the NIST had lower transit time and lower dark current advantages over the as-grown ISU. The relative advantage of the ISU structure was prefabrication tunable operation wavelength and adjustable absorption layer thickness.

According to photoresponse simulations, the ISU structure should yield a higher quantum efficiency, as compared to the NIST structure. However, our measurements have shown that the NIST samples had 50% peak quantum efficiency, larger than 47% of that of the ISU samples. Most probable causes of lower efficiency of ISU samples, as compared to our simulations, are scattering losses at the rough Schottky surface and some current loss mechanisms inherent

in the device structure.

High speed measurements were setup limited. Theoretical fits to experiments predict over 78 GHz bandwidth for the NIST samples. ISU samples, with three different possible absorption layer thicknesses, has bandwidths of 51 GHz, 71 GHz and 110 GHz for the S1, S2, and S3 samples, respectively. To the best of our knowledge, the S3 sample is the fastest of its class, and has the highest bandwidth-efficiency products in the scientific literature, excluding noisy APDs.

Further increase in the quantum efficiency can be achieved by optimizing some fabrication parameters. Replacing the top silicon nitride layer by $\lambda/4$ silicon nitride/silicon dioxide distributed Bragg reflectors (DBR) will increase the reflectivity of top the mirror.[43] According to RCE theory this will increase the efficiency of the photodiodes. A recipe developed for this top layer Bragg mirror have already showed promising results. However, introduction of this top Bragg mirror will cause more complicated subsequent processes. Especially, the dielectric etch process is likely to cause some isotropic etch problems.

Although the gold Schottky contact acts as a good top mirror, it also scatters and absorbs a great fraction of the optical power. Introducing a more transparent indium tin oxide (ITO) Schottky material instead of gold, promises higher quantum efficiencies.[44] Combined with top DBR effect, the quantum efficiency is expected to increase remarkably, for both structures. Our first trials of ITO based Schottky diodes have been promising.

Another achievement could be the planarization of the devices, by means of introducing isolation by proton implantation, instead of the mesa etch. This implantation results in nonconducting epilayers, which is required for isolation purposes and for low loss dielectric medium of the CPW transmission lines. The advantage of planarization is better uniformity, easier fabrication processes, and higher resolution for the following fabrication steps.[36] A new mask group for this modified process has been designed and is ready for oncoming processes. We have already developed a process for proton implantation level and our first test was successful.

Apart from enhancing bandwidth-efficiency of the 840 nm, the know-how

has accumulated well enough to start fabrication of photodiodes for longer wavelengths, at first hand for 1.55 μm. InAs/InSb material family is suitable for the photodetection of 1.5-5.0 μm wavelengths, which finds many scientific, industrial, and military applications.[45] Process development for this structure has been started.

These plans are for near future, but in the rapidly developing world of photonics who can ever guess what is behind the next door?

Bibliography

[1] F. Braun, *Pogg. Ann.*, 153, p 556, 1874.

[2] G. W. Pickard, *US. patent No. 836531*, 1906.

[3] E. H. Rhoderick and R. H. Williams, *Metal-semiconductor contacts*, Second Edition, Clarendon Press, Oxford, 1988.

[4] H. C. Huang, "A novel millimeter-wave gallium arsenide beam-lead mixer diode with cutoff frequency >2 THz," *Canadian J. Phys.*, vol. 69, no. 3-4, pp. 180-184, 1991.

[5] T. W. Crowe, "GaAs Schottky barrier mixer diodes for the frequency range 1-10 THz," *Int. J. Infrared and Millimeter Waves*, vol. 11, no. 7, pp. 765-777, 1989.

[6] R. U. Titz, "Investigation of GaAs Schottky barrier diodes in the THz range," *Int. J. Infrared and Millimeter Waves*, vol. 11, no 7, pp. 809-820, 1990.

[7] A. Raisenen, "Capability of Schottky-diode multipliers as local oscillators at 1 TIIz," *Microwave and Optical Tech. Lett.*, vol. 4, no. 1, pp. 29-33, 1991.

[8] E. Ahlstrom and W. W. Gartner, "Silicon surface-barrier photocells," *J. Appl. Phys.*, vol. 33, p. 2602, 1962.

[9] M. V. Schneider, "Schottky barrier photodiodes with antireflection coatings," *Bell Syst. Tech. J.*, vol. 45, p. 1611, 1966.

[10] S. Y. Wang and D. M. Bloom, "100 GHz bandwidth planar GaAs Schottky photodiode," *Electron. Lett.*, vol. 19, no. 14, pp. 554-555, 1983.

[11] D. G. Parker, P. G. Say, A. M. Hanson, and W. Sibbett, "110 GHz high efficiency photodiodes fabricated from indium tin oxide/GaAs," *Electron. Lett.*, vol. 23, pp. 527-528, 1983.

[12] E. Özbay, K. D. Li, and D. M. Bloom, "2.0 psec GaAs monolithic photodetector and all electronic sampler," *IEEE Photonics Tech. Lett.*, vol. 3, no. 6, pp. 570- 572, 1991.

[13] M. S. Ünlü and S. Strite, "Resonant cavity enhanced photonic devices," *J. Appl. Phys. Rev.*, vol. 78, pp. 607-639, 1995.

[14] H. Nie, K. A. Anselm, C. Hu, S. S. Murtaza, B. G. Streetman, and J. C. Campbell, "High-speed resonant cavity separate absorption and multiplication avalanche photodiodes with 130 GHz gain-bandwidth product," *Appl. Phys. Lett.*, vol. 69, pp. 161-163, 1996.

[15] H. Nie, K. A. Anselm, C. Lenox, P. Yuan, C. Hu, G. Kinsey, B. G. Streetman, and J. C. Campbell, "Resonant-Cavity Separate Absorption, Charge and Multiplication Avalanche Photodiodes With High-Speed and High Gain-Bandwidth Product," *IEEE Photonics Tech. Lett.*, vol. 10, no. 10, pp. 409-411, 1998.

[16] D. C. Diaz, C. L. Schow, J. Qi, J. C. Campbell, J. C. Bean, and L. J. Peticolas, "Si/SiO2 resonant cavity photodetector," *Appl. Phys. Lett.*, vol. 66, pp. 2798-2800, 1996.

[17] S. F. Lim, G. S. Li, W. Yuen, C. J. Chang-Hasnian, "Intracavity resonant quantum-well photodetection of a vertical-cavity surface emitting laser," *Electron. Lett.*, vol. 33, pp. 597-598, 1997.

[18] G. S. Li, W. Yuen, and C. J. Chang-Hasnian, "Wide and continuously tunable (30 nm) detector with uniform characteristics over tuning range," *Electron. Lett.*, vol. 33, pp. 1122-1124, 1997.

[19] S. Y. Hu, J. Ko, L. A. Coldren, "Resonant-cavity InGaAs/InAlGaAs/InP photodetector arrays for wavelength demultiplexing applications," *Appl. Phys. Lett.*, vol. 70, pp. 2347-2349, 1997.

[20] C. C. Barron, C. J. Mahon, B. J. Thibeault, G. Wang, W. Jiang, L. A. Coldren, and J. E. Bowers, "Resonant-cavity-enhanced pin photodetector with 17 GHz bandwidth efficiency product," *Electron. Lett.*, vol. 30, pp. 1796-1797, 1994.

[21] A. Strittmatter, S. Kollakowski, E. Droge, E. H. Bottcher, D. Bimberg, "High speed, high efficiency resonant cavity enhanced InGaAs MSM photodetectors," *Electron. Lett.*, vol. 32, pp. 1231-1232, 1996.

[22] K. Xie, J. H. Zhao, Y. Shi, H. Lee, G. Olsen, "Resonant cavity enhanced GaInAsSb-AlAsSb photodetector grown by MBE for mid-IR applications," *IEEE Photonics Tech. Lett.*, vol. 8, pp. 667-669, 1996.

[23] M. S. Ünlü and H. P. Zengingönül, "Polarisation sensing with resonant cavity enhanced photodetectors," *Electron. Lett.*, vol. 32, pp. 591-592, 1996.

[24] A. Chin and T. Y. Chang, "Multilayer reflectors by molecular-beam epitaxy for resonance enhanced absorption in thin high-speed detectors," *J. Vac. Sci. Tecnol. B*, vol 8., pp. 339-342, 1990.

[25] Y. Tzeng, S. Li, and P. Ho, "A GaAs Schottky-barrier photodiode with high quantum efficiency-bandwith product by using a multilayer reflector," *IEEE Trans. Electron Devices.*, vol. 40, pp. 348-352, 1993.

[26] E. Özbay, M. S. Islam, M. Gökkavas, O. Aytür, and M. S. Ünlü, "High-speed resonant cavity enhanced Schottky photodiodes," *IEEE Photonics Tech. Lett.*, vol. 9, pp. 672-674, 1997.

[27] M. S. Ünlü, M. Gökkavas, B. M. Onat, E. P. Ata, E. Özbay, R. P. Mirin, K. J. Knopp, K. A. Bertness, and D. H. Christensen, "High bandwidth-efficiency resonant cavity enhanced Schottky photodiodes for 800-850 nm wavelength operation," *Appl. Phys. Lett.*, vol. 72, pp. 2727-2729, 1998.

[28] B. M. Onat, M. Gökkavas, E. Özbay, E. P. Ata, E. Towe, and M. S. Islam, "100-GHz Resonant Cavity Enhanced Schottky Photodiodes," *IEEE Photon. Technol. Lett.*, vol. 10, pp. 707-709, 1998.

[29] S. M. Sze, *Physics of Semiconductor Devices*, Second Edition, Wiley, New York, 1981.

[30] A. M. Joshi and G. H. Olsen, Ch.16: Photodetection, in *Handbook of Optics* (ed. M. Bass), Second Edition, McGraw-Hill, New York, 1995.

[31] J. E. Bowers and Y. G. Wey, Ch. 17: High Speed Photodetectors, in *Handbook of Optics* (ed. M. Bass), Second Edition, McGraw-Hill, New York, 1995.

[32] H. H. Tung and C.P. Lee, "Design of a resonant-cavity-enhanced photodetector for high-speed applications," *IEEE J. Quantum Electron.*, vol. 33, pp. 753-760, 1997.

[33] Y. G. Wey, K. S. Giboney, J. E. Bowers, M. J. Rodwell, P. Silvestre, P. Thiagarajan, and G. Y. Robinson, "110 GHz GaInAs/InP p-i-n Photodiodes with Integrated Bias Tees and Matched Resistors," *IEEE Photonic Tech. Lett.*, vol. 5, pp. 1310-1312, 1993.

[34] Mutlu Gökkavas, *Design and characterization of RCE photodetectors*, Bilkent University M. Sc. Thesis, 1996.

[35] Y. J. E. Bowers and C. A. Burrus, "Ultrawide-Band Long-Wavelength p-i-n Photodetectors," *J. Lightwave Technol.*, vol. LT-5, pp. 1339-1350, 1987.

[36] R. E. Williams, *Modern GaAs Processing Methods*, Second Edition, Artech House, Boston, 1990.

[37] M. S. Islam, *Fabrication and characterization of high speed resonant cavity enhanced Schottky photodiodes*, Bilkent University M. Sc. Thesis., 1996.

[38] William S. Rees (ed.), *CVD of non-metals*, Weinheim, New York,1996.

[39] R. E. Collin, *Foundations for Microwave Engineering*, Mc. Graw-Hill, Singapore, 1966.

[40] P. Yeh, *Optical Waves in Layered Media*, Wiley-Interscience, New York, 1988.

[41] K. Li Dessau, *Insights into high-speed detectors and high frequency detectors*, Application Note 1, New Focus Inc., Mountain View, CA.

[42] R. Thomas Hawkins II, Micheal D. Jones, Steven H. Pepper, and Jeffrey H. Goll, "Comparison of fast photodetector response measurements by optical heterodyne and pulse response techniques," *IEEE J. Lightwave Technol.*, vol. 9, pp. 1289-1294, 1991.

[43] S. S. Murtaza, K. A. Anselm, A. Srinivasan, B. G. Streetman, J. C. Campbell, J. C. Bean, and L. Peticolas, "High-reflectivity Bragg mirrors for optoelectronic applications," *IEEE J. Quantum Electron.*, vol. 31, pp. 1819-1825, 1995.

[44] W. Gao, P. R. Berger, R. G. Hunsperger, G. Zydzik, W. W. Rhodes, H. M. O'Bryan, D. Sivco, and A. Y. Cho, "Transparent and opaque Schottky contacts on undoped $In_{0.52}Al_{0.48}As$ grown by molecular beam epitaxy," *Appl. Phys. Lett.*, vol. 66, pp. 3471-3473, 1995.

[45] F. Mansoor, S. K. Haywood, N. J. Mason, R. J. Nicholas, P. J. Walker, R. Grey, and G. Hill,"Resonant cavity-enhanced (RCE) photodetector based on Ga(In)Sb for gas-sensing applications," *Semicond. Sci. Technol.*, vol. 10, pp. 1017-1021, 1995.